Time Resolved Measurements on Diffusion of Light

Ivo Vellekoop

Time Resolved Measurements on Diffusion of Light

Ivo M. Vellekoop

Graduation Thesis
November 21, 2003

Complex Photonic Systems (COPS) Group
Faculty of Science and Technology

Integrated Optical MicroSystems (IOMS) Group
Faculty of Electrical Engineering, Mathematics and Computer Science

Graduation Committee

Prof. Dr. A. Lagendijk (COPS)
Dr. P. Lodahl (COPS)
Drs. B.P.J. Bret (COPS)
Prof. Dr. A. Driessen (IOMS)
Dr. Ir. R.M. de Ridder (IOMS)

Contents

Chapter 1

Introduction

1.1 Diffusion and physics

In language 'diffuse' means vague, featureless and without a clear direction. The meaning of the word is almost the same in physics. Diffusion denotes the process of uniform spreading caused by random movement, it is a general principle that has applications in almost all fields of physics.

An everyday example of this principle is diffusion of odors. When a bottle of perfume is left open, at first the fragrance is concentrated around the bottle, but slowly the scent starts to fill the whole room. The mechanism behind this is a statistical one. Because the molecules in the air move randomly, they will push the perfume molecules in random directions. The more molecules there are in a certain volume, the more will be pushed out of this volume. Therefore on average the molecules are pushed towards areas with a lower concentration, which ultimately causes concentration differences to disappear. Exactly the same thing happens when a drop of ink is put in a glass of water; eventually all water will have the same color.

Diffusion of gasses and fluids is just the beginning. Electrons can diffuse in a conductor, heat diffuses according to the laws of thermodynamics, a crowd diffuses after a demonstration and even vegetation diffuses. The common denominator in these processes is that a large number of seemingly random interactions cause a concentration difference to decrease.

1.2 Diffusion of waves

Waves, like sound or light, can also experience diffusion. The random interaction is caused by a disordered configuration of particles that disturb the propagation of the wave. Such particles are called scatterers. The most important difference between waves and particles is that waves can interfere; if two waves are added together, they can increase or diminish each other, depending on their relative phase. Due to the random position of the scatterers, a complicated spatial pattern called speckle arises. In dynamic diffusion experiments also temporal interference effects (time speckle) can be seen.

Because of interference, diffusion of waves differs from diffusion of particles. Although particle diffusion theory forms a good approximation for the diffusion of light, some very

interesting phenomena are missed in this description.

The most far-reaching of these phenomena is Anderson localization of light. In 1953, P.W. Anderson predicted that diffusion of electrons in a random lattice is stopped completely when the scattering is strong enough [1]. This effect was predicted to occur for light as well when the scattering of light is extremely strong [2, 3]. Due to the resulting interference, the propagation of light is disturbed to such an extent that light travels around in closed loops and is said to be localized.

1.3 History

So far several features unique to wave diffusion have been established experimentally using stationary intensity measurements. One of these features is enhanced backscattering [4, 5, 6, 7, 8]. Because of this effect more light is scattered back to the source than what would be expected from particle diffusion theory. Other measurements confirmed predictions about intensity correlations in strongly scattering materials [9].

Experimental prove of the ultimate interference effect, Anderson localization, has been reported [10, 11]. These claims, however, have been questioned because absorption can produce similar effects [12]. Both static transmission measurements and enhanced backscattering measurements provide us only with time averaged values. As a result, localization cannot easily be distinguished from absorption and no information about the dynamics of the process can be obtained.

For this reason, a dynamic measurement technique has been developed [13]. This technique allows a dynamic measurement of the intensity of light that propagated through a random medium. From this information the diffusion constant, which quantifies the rate of diffusion in a random medium, can be found [14, 15]. Moreover, the setup can be used to measure the phase of the light. Analysis of the phase information gives access to a whole new dimension in the analysis of wave propagation and is able to uniquely identify signs of Anderson localization [16, 17].

Recently a theory describing the statistical properties of the phase has been developed [18]. This theory is in good agreement with experiments using microwave radiation [19, 20]. Similar promising experiments have been performed in the optical domain [21]. These experiments were performed on strongly scattering gallium phosphide samples and confirmed the predictions for transmitted light. For reflected light, however, a deviation from the predicted behavior was found.

A full understanding of the measurement technique and the theory of phase statistics is required to be able to identify signs of localization in the phase information. For this reason, measurements will have to be performed on less strongly scattering materials. The propagation of light in these samples can be explained very well using the model of particle diffusion or the more detailed radiative transfer approach [22]. This way the limitations and possibilities of the method can be investigated without having to worry about the complications of strong localization. Only after this technique has thoroughly been characterized and all pitfalls have been tracked down it can be used to study strong scattering and possibly localization.

1.4 Project goals

The main goal of this project is to identify the possibilities and limitations of the time-resolved measurement technique, paving the road for future experiments on samples that may exhibit localization. For this purpose time-resolved measurements will be performed on well characterized samples that are known to be relatively far away from Anderson localization. Both the measurement setup and the data analysis will be scrutinized to make sure neither the measurement setup nor the data processing introduce artefacts.

The second project goal is to study the application of existing multiple scattering theory in the analysis of the dynamic measurements. Multiple scattering theory describes the propagation of light in random media and can be used to predict the outcome of the time-resolved measurements. If we want to be able to interpret the results of the measurements, we have to understand how this theory works and what assumptions and simplifications are behind it. Special attention will be given to predictions governing the statistics of the phase of multiple scattered light [18]. The results from this new phase analysis technique will be compared to the results from intensity measurements, both theoretically and experimentally. Furthermore, as suggested in [21], effects of the surfaces of the samples will be examined in detail.

1.5 Overview of the thesis

The thesis consists of two parts. The first part, consisting of the chapters 2 and 3, forms a theoretical background for the experiment. Chapter 2 introduces a formalism to handle multiple scattering statistically. Starting with a scalar wave-equation the theory is simplified and abstracted until a simple graphical representation is the result. In Chapter 3 this formalism is used to derive the diffusion equation for light. The diffusion equation is used to predict the dynamics of a pulse transmitted through a slab of random material. Furthermore, the phase statistics that was introduced in [18] is examined in detail and the theory is improved to include boundary effects.

In order to improve the readability of these two theoretical chapters some of the more elaborate derivations are put in appendices. These derivations can be skipped without problem, but are included for completeness.

The second part of the thesis focusses on the experiment. In this part the results of the phase measurements and of the intensity measurements are presented and compared. Chapter 4 describes the setup and the data analysis in detail. Data processing is an important aspect of the experiment since distortions are introduced easily. Therefore the procedure required to extract the right information from the measurement is clarified using real data. Finally the results of measurements on a set of samples with different thicknesses are presented in Chapter 5. The results are used to identify trends and to test for deviations from diffusion theory.

In the final chapter conclusions are drawn concerning the applicability of the setup and the trends that were found in the experiments. The time-resolved measurement setup is found to be widely usable and several suggestions for future experiments will be made.

Chapter 2

Multiple scattering of light

2.1 Introduction

In this chapter a theoretical framework for describing the propagation of light in random media is presented. The theory in this chapter is not new but serves as an introduction to the multiple scattering formalism and forms a basis for Chapter 3, where the theoretical background of the experiments is laid out. More information on multiple scattering theory can be found in [22, 9, 23].

A random medium is modeled as a collection of scattering particles between which light bounces back and forth, very similar to the way a ball bounces in a pinball machine. Since the distribution of these scatterers is random, a statistical analysis of the light propagation is required.

First propagation of light through a homogeneous medium will be studied and the Green function formalism will be introduced. In the next section, this formalism will be adapted to describe propagation in inhomogeneous media.

Although in principle the propagation of light through any medium can be described using this method, most of the times it is not possible to analytically solve the equations. A huge simplification is required and is found in modeling the material as a collection of points scattering light.

The statistical treatment of randomness is treated in Section 2.4. A method for averaging over disorder in a random medium is laid out and a graphical representation of the averaging process is introduced. This diagrammatic method will be used to calculate the expectation value of the field in a random medium. In Chapter 3 the diagrams will prove useful again.

In Section 2.5, it is shown how the propagation of light through a random medium can be described by an effective refractive index and a mean free path. Finally, the limit of a high number of weak scatterers is calculated to show that this gives a microscopic model for the refractive index of a material.

2.2 Light propagation in homogeneous media

In this section unscattered propagation of light will be described using a wave equation and a corresponding Green function will be derived. The Green function approach will be

used throughout this thesis to describe propagation of light.

2.2.1 Wave equation

The electrical and magnetic fields are vector quantities. For practical purposes, however, it is easier to find solutions for a scalar representation of the electromagnetic field. If desired, vector solutions can be calculated from these scalar solutions [24]. Propagation of light in a homogeneous medium can be described by the scalar Helmholtz wave equation,

$$-\nabla^2\Psi(\mathbf{r}) - k^2\Psi(\mathbf{r}) = 0, \tag{2.1}$$

where Ψ is the complex amplitude of the electrical field and $k = n\omega/c$. In this equation n is the refractive index of the material, ω and c are the angular frequency and speed of light in vacuum respectively.

Assumption: *The medium is source free, linear, isotropic and homogeneous. This is true for air or free space* ($n = 1$) *and a good approximation for most materials if the the intensity is not too high. With this assumption, Eq.* (2.1) *can be derived from the Maxwell equations.*

2.2.2 Green function

The Green function of the electrical field is the solution to the wave equation in the presence of a point source at position $\mathbf{r}'$. For a medium without scatterers we have the bare Green function g,

$$-\nabla^2 g(\mathbf{r}, \mathbf{r}') - k^2 g(\mathbf{r}, \mathbf{r}') = \delta(\mathbf{r} - \mathbf{r}'). \tag{2.2}$$

The Green function is the spatial impulse response of the system. It describes propagation of light and therefore sometimes is called a propagator. Once it is known, the response to an arbitrary source $\Psi_s(\mathbf{r})$ can be found by multiplying $g(\mathbf{r}, \mathbf{r}')$ with the source term and integrating over the whole space.

$$\Psi(\mathbf{r}) = \int d\mathbf{r}' g(\mathbf{r}, \mathbf{r}')\Psi_s(\mathbf{r}') \tag{2.3}$$

Since the medium is homogeneous, $g(\mathbf{r}, \mathbf{r}') = g(\mathbf{r} - \mathbf{r}')$ which will sometimes be written $g(\mathbf{r})$. The Green function can be found by spatially Fourier transforming equation (2.2), introducing the wave-vector coordinate $\mathbf{p}$ as the transform parameter,

$$(p^2 - k^2)g(\mathbf{p}) = 1, \tag{2.4}$$

$$g(\mathbf{p}) = \frac{1}{p^2 - k^2 + i\epsilon}. \tag{2.5}$$

The $i\epsilon$ term is an infinitesimally small offset that is added to fix the divergence at $p = k$. This offset allows transforming this equation back to real space, which is described in detail in Appendix A.1,

$$g(\mathbf{r}) = -\frac{e^{ikr}}{4\pi r}. \tag{2.6}$$

The real-space Green function corresponds to a spherical wave emitted from the origin, oscillating with a spatial frequency k. The amplitude of the electrical field falls of with $1/r$.

2.3 Light propagation in inhomogeneous media

2.3.1 The scattering potential

Scattering is the process where a contrast in refractive index causes light to be reflected in different directions. The difference in refractive index can be expressed as a potential $V(\mathbf{r}) \equiv [n^2(\mathbf{r}) - n_0^2]\omega^2/c^2$. With help of this potential, the wave equation for an inhomogeneous medium can be written,

$$-\nabla^2\Psi(\mathbf{r}) - k^2\Psi(\mathbf{r}) = V(\mathbf{r})\Psi(\mathbf{r}), \tag{2.7}$$

where $k = n_0\omega/c$. For this wave equation again a Green function can be defined. This is the full Green function G,

$$-\nabla^2 G(\mathbf{r}, \mathbf{r}') - k^2 G(\mathbf{r}, \mathbf{r}') = V(\mathbf{r})G(\mathbf{r}, \mathbf{r}') + \delta(\mathbf{r} - \mathbf{r}'). \tag{2.8}$$

The full Green function has a relation with the bare Green function. A recursive definition can be found by treating the right hand side of (2.8) as a source term and applying (2.3). This yields,

$$G(\mathbf{r}, \mathbf{r}') = g(\mathbf{r} - \mathbf{r}') + \int d\mathbf{r}_1 g(\mathbf{r} - \mathbf{r}_1)V(\mathbf{r}_1)G(\mathbf{r}_1, \mathbf{r}'), \tag{2.9}$$

which is called the Dyson-Schwinger equation. It relates the propagation, G, to unscattered propagation, g, and scattering potential V in a recursive way.

2.3.2 Point scattering

The point scattering model is a simplification to the exact Dyson-Schwinger equation. (2.9). It assumes that the effect of a finite size scatterer with a finite refractive index can be modeled as a point with an infinite refractive index (a delta function). The point scatterers are assumed to be isotropic, meaning they scatterer light equally in all directions.

Assumption: *Scattering is isotropic and the scattering medium can be modeled by discrete scatterers.*

The point scattering model allows discretization of Eq. (2.9). The strength of scatterer i is represented by V_i,

$$G(\mathbf{r}, \mathbf{r}') = g(\mathbf{r} - \mathbf{r}') + \sum_{i=1}^{N} g(\mathbf{r} - \mathbf{r}_i)V_i G(\mathbf{r}_i, \mathbf{r}'). \tag{2.10}$$

This discrete Dyson-Schwinger equation can be seen as a summation of different propagation paths. The first part describes unscattered propagation. The summed terms describe paths that have scatterer i as the last scattering event. Light first propagates

through the scattering medium from the source $\mathbf{r}'$ to the last scatterer $\mathbf{r}_i$ as described by the full Green function $G(\mathbf{r}_i, \mathbf{r}')$. Then it is scattered with strength V_i and travels undisturbed to point $\mathbf{r}$.

2.3.3 The T-matrix

As can be seen from Eq. (2.10), the full Green function G is defined as a sum of terms containing the same function G. The T-matrix formalism is a method of breaking this recursion.

Recognizing that the Green function $G(\mathbf{r}_i, \mathbf{r}')$ represents the sum of all paths from $\mathbf{r}'$ to $\mathbf{r}_i$, a decomposition can be made to isolate the effect of scatterer i. If $G_i(\mathbf{r}, \mathbf{r}')$ is defined as the sum of all paths that do not include scattering on i, the full Green function can be expanded as an infinite sum,

$$G(\mathbf{r}, \mathbf{r}') = G_i(\mathbf{r}, \mathbf{r}') + G_i(\mathbf{r}, \mathbf{r}_i)V_iG_i(\mathbf{r}_i, \mathbf{r}') + G_i(\mathbf{r}, \mathbf{r}_i)V_iG_i(\mathbf{r}_i, \mathbf{r}_i)V_iG_i(\mathbf{r}_i, \mathbf{r}') + \dots . \quad (2.11)$$

The interpretation of this expansion is that light can propagate without scattering on i, it can scatter there once, it can scatter once and return to scatter a second time and so on. The term $V_iG(\mathbf{r}_i, \mathbf{r}')$ in Eq. (2.10) can be rewritten,

$$V_iG(\mathbf{r}_i, \mathbf{r}') = \frac{V_i}{1 - V_iG_i(\mathbf{r}_i, \mathbf{r}_i)}G_i(\mathbf{r}_i, \mathbf{r}') \equiv T_iG_i(\mathbf{r}_i, \mathbf{r}'), \quad (2.12)$$

where T_i is called the T-matrix* for scatterer i. The significance of this method is that once T_i is known, the full Green function for a medium with N scatterers can be written in terms of the Green function for a medium without this scatterer, thus containing $N-1$ scatterers. The T-matrix describes scattering from a particle taking into account all other scatterers in the medium.

In a system where the scatterers are not very close to each other, the T-matrix of a scatterer is not influenced much by the presence of other scatterers. Therefore the Green function of the environment can be approximated by the bare Green function and the T-matrix is replaced by t, the T-matrix for a single scatterer in free space.

Approximation: *The matrix T corresponding to scattering in a disordered environment is replaced by t, the matrix for a single scatterer in free space. This is called the independent scattering approximation.*

$$t_i \equiv \frac{V_i}{1 - V_ig(0)} \quad (2.13)$$

Since $g(\mathbf{r})$ diverges at $\mathbf{r} = 0$, this definition of the t-matrix poses a problem. To fix this problem, a regularized Green function is introduced. This function has a finite value at $\mathbf{r} = 0$ and models resonances that would occur in a finite size scatterer. The regularization

*In the continuous case, T is a function of two coordinates and represents scattering from one point in the scatterer to another. Because there are two coordinates in T it is called a (continuous) matrix. The continuous representation of a single point-scatterer is $T(\mathbf{r}, \mathbf{r}') = T_i\delta(\mathbf{r}_i - \mathbf{r})\delta(\mathbf{r}_i - \mathbf{r}')$, which is a diagonal matrix.

procedure is described in detail in Appendix A.2. Since the regularized Green function is a function of ω, the t-matrix will be frequency dependent. Now Eq.(2.10) can be rewritten,

$$G(\mathbf{r},\mathbf{r}') = g(\mathbf{r}-\mathbf{r}') + \sum_{i=1}^{N} g(\mathbf{r}-\mathbf{r}_i)t_i(\omega)G_i(\mathbf{r}_i,\mathbf{r}'). \tag{2.14}$$

Although the differences between equations (2.10) and (2.14) appear minimal, in the latter resonances of a finite scatterer are taken into account and the effect of a single scatterer is separated from the effect of the surrounding scatterers. This will be of particular use in the next section where the randomness of a material is treated statistically.

2.4 Disorder

Equation (2.14) describes scattering on one or more scatterers at known positions. For random media, however, the distribution of scatterers is not known. In principle every configuration is possible. The probability to have a particular configuration is defined $P(\mathbf{r}_1,\ldots,\mathbf{r}_N)$, where r_n is the position of the n^{th} scatterer. We introduce the ensemble average operator for averaging over realizations of the random medium,

$$\langle\cdot\rangle \equiv \int d\mathbf{r}_1\ldots d\mathbf{r}_N\, P(\mathbf{r}_1,\ldots,\mathbf{r}_N)\,[\cdot]\,, \tag{2.15}$$

where $[\cdot]$ represents a quantity that depends on the realization of the medium. The averaging operator can be applied to the full Green function to determine the expectation value of G. This quantity is called the amplitude or average Green function,

$$\big\langle G(\mathbf{r},\mathbf{r}')\big\rangle = g(\mathbf{r}-\mathbf{r}') + \sum_{i=1}^{N} t_i(\omega)\int d\mathbf{r}_1\ldots d\mathbf{r}_N\, P(\mathbf{r}_1,\ldots,\mathbf{r}_N)g(\mathbf{r}-\mathbf{r}_i)G_i(\mathbf{r}_i,\mathbf{r}'), \tag{2.16}$$

where $g(\mathbf{r}-\mathbf{r}')$ and $t_i(\omega)$ were taken out of the averaging operator since they do not depend on the position of the scatterers. Since $g(\mathbf{r}-\mathbf{r}_i)$ only depends on $\mathbf{r}_i$, it can be taken out of all integrations except the integration over $\mathbf{r}_i$,

$$\big\langle G(\mathbf{r},\mathbf{r}')\big\rangle = g(\mathbf{r}-\mathbf{r}') + \sum_{i=1}^{N} t_i(\omega)\int d\mathbf{r}_i\, P(\mathbf{r}_i)g(\mathbf{r}-\mathbf{r}_i)\left\langle G_i(\mathbf{r}_i,\mathbf{r}')|\mathbf{r}_i\right\rangle, \tag{2.17}$$

where operator $\langle\cdot|\mathbf{r}_i\rangle$ stands for averaging over all scatterer positions except that of scatterer i, which is given. If the scatterer positions are independent, the Green function G_i of the environment of i does not depend on $\mathbf{r}_i$ and therefore $\langle G_i|\mathbf{r}_i\rangle = \langle G_i\rangle$. This is the average Green function for a medium with one scatterer less than the medium that is under investigation. The higher the number of scatterers, the closer $\langle G_i\rangle$ will be to $\langle G\rangle$. Assuming there are many scatterers, $\langle G_i\rangle$ can be approximated by $\langle G\rangle$. All this can be represented by a very simple diagram, shown in figure 2.1. Because diagrams are far easier to read than the corresponding equations, they are an insightful way to manipulate equations. In Chapter 3 the same diagrammatic technique will be used to describe the more complex intensity propagator.

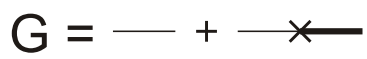

Figure 2.1: Diagrammatic representation of the averaging process described in Eq.(2.17)*. Thin lines corresponds to the bare propagators, g. The cross represents the t-matrix of the last scatterer (t_i in the equation) and the thick line corresponds to the full Green function of the scatterer's environment, $\langle G_i|\mathbf{r}_i\rangle$, which will be approximated by $\langle G\rangle$. In the equation it can be seen that the second term of the diagram should be averaged over the position of the scatterer and summed over all scatterers. It is customary not to show this in the diagram explicitly.*

Assumption: *The positions of the scatterer are statistically independent and have a uniform distribution in an infinite medium. The number of scatterers is high enough to approximate G_i by G.*

For an infinite medium with a uniform density of scatterers n, the absolute space dependence in the average Green function disappears. Defining $t \equiv \sum_{i=1}^{N} t_i/N$ the average Green function can be written,

$$\left\langle G(\mathbf{r}-\mathbf{r}')\right\rangle = g(\mathbf{r}-\mathbf{r}') + nt(\omega)\int d\mathbf{r}_i\, g(\mathbf{r}-\mathbf{r}_i)\left\langle G(\mathbf{r}_i-\mathbf{r}')\right\rangle, \tag{2.18}$$

which can be solved by Fourier transforming with respect to $\mathbf{r}-\mathbf{r}'$,

$$\langle G(\mathbf{p})\rangle = g(\mathbf{p}) + nt(\omega)g(\mathbf{p})\langle G(\mathbf{p})\rangle \tag{2.19}$$

$$\langle G(\mathbf{p})\rangle = \frac{1}{g^{-1}(\mathbf{p}) - nt(\omega)} = \frac{1}{p^2 - k^2 - nt(\omega)} \tag{2.20}$$

This result can be written in the same form as the bare Green function with $K(\omega)^2 \equiv k^2 + nt(\omega)$ and transformed to real space.

$$\langle G(\mathbf{r},\omega)\rangle = -\frac{e^{iK(\omega)r}}{4\pi r} \tag{2.21}$$

The average Green function is again a spherical wave emitted from the origin. The effect of multiple scattering is incorporated in the effective wavevector K, which is frequency dependent because the t-matrix for a scatterer is.

2.5 Coherent propagation

Transport of light through a material can be expressed in terms of the wavevector k. The real part of the wavevector describes propagation, the imaginary part corresponds to extinction. In homogeneous materials extinction is caused by absorption.

Likewise, the ensemble averaged propagation of the field, which is named coherent propagation, can be expressed in terms of the effective wavevector K. An important property of coherent propagation is that its direction is the same as for unscattered propagation, the only differences being the propagation velocity and the extinction, both accounted for by the effective wavevector.

As opposed to propagation in a uniform medium, the extinction of the coherently propagating field is not only caused by absorption but also by scattering. Even if the scattering process is energy conserving it causes the direction and phase of the light to become randomized, thus decreasing the average amplitude of the field.

It is useful to define an effective refractive index n_{eff} and an extinction mean free path ℓ_{ex} that can be calculated from the effective wavevector.

$$K \equiv \sqrt{k^2 + nt} \equiv k_0 n_{\text{eff}} + \frac{i}{2\ell_{\text{ex}}}, \tag{2.22}$$

where $k_0 \equiv \omega/c$. Without absorption, ℓ_{ex} equals the scattering mean free path ℓ_{sc}. This is the length-scale over which light is scattered out of an incoming beam. In the case of isotropic scattering, this length equals the transport mean free path ℓ. The transport mean free path corresponds to the distance that light can travel before the direction is randomized.

Assumption: *Scattering is isotropic and there is no absorption, hence* $\ell_{ex} = \ell_{sc} = \ell$

Even more important than the coherent phase velocity $v_\phi \equiv \omega/\text{Re}\{K\} = c/n_{\text{eff}}$ is the group velocity v_{gr}. This velocity is defined,

$$v_{\text{gr}} \equiv \frac{1}{\text{Re}\{dK/d\omega\}}. \tag{2.23}$$

The group velocity is the velocity at which the envelope of a pulse of light propagates through the scattering material. The separate frequency components travel at the phase velocity.

2.5.1 Small scatterer limit

The point scattering model is applicable when the scatterers are small with respect to the wavelength of the light, there is no lower limit to the scatterer size. In fact, the point scattering model describes scattering by atoms very well and can be used to model a homogeneous dielectric. To do so, the limit of a very high density of very weak scatterers is taken. The product nt is given by Eq.(2.13),

$$nt = \frac{nV}{1 - VG(0)}, \tag{2.24}$$

here V is the optical potential integrated over the volume of the scatterer and is proportional to a^3, where a is the radius of the scatterer. The density of scatterers, n, is inversely proportional to a^3 and $G(0)$ scales with a^{-1} as is shown in Appendix A.2. In the limit of very small scatterers, a goes to zero, $VG(0) \ll 1$ and $nt = nV$. In absence of absorption this is a real, positive value and therefore K is real. A real valued wavevector describes propagation without extinction, so this means that multiple scattering between randomly ordered atoms composing a dielectric material effectively amounts having a single refractive index for the material.

2.6 Summary

In this chapter the propagation of light through a random multiply scattering medium was studied. First, the material was modeled as a collection of points scattering light. The t-matrix was introduced to describe scattering on a single scatterer. This discretized description of the material was used to handle randomness.

In random materials the propagation of the electrical field could be calculated only in an average sense, where the average is over all possible scatterer configurations. Making use of the t-matrix formalism, the averaging process was described by a simple diagram. This method can be extended to the more complicated case of propagation of light intensity, which will be done in the following chapter.

It was seen that the expectation value of the propagating electrical field inside a random material, the so called coherent propagation, can be described the same way as the propagating field in a homogeneous lossy medium. This was achieved by replacing the wavevector in vacuum by an effective wavevector, describing both propagation and extinction by scattering. Measurements showing the coherent beam will be presented in Chapter 5. Finally, the point scatterer formalism was shown to describe regular propagation through a homogeneous dielectric when the scatterers are small enough.

Chapter 3

Field fluctuations

3.1 Introduction

In the previous chapter the average propagator for the electrical field in a random medium was calculated. One could think that this propagator is sufficient to fully describe light propagation in a random medium. However, in this description there is no information about how the field in an actual sample deviates from the average field. The field in the medium varies depending on the exact configuration of scatterers. These variations as a function of random realization are called fluctuations. Fluctuations have a spatial pattern and a temporal pattern; these patterns are referred to as speckle. Concretely the term speckle means that the field deviates from the expectation value in a random way and the speckle pattern is different for every sample.

In this chapter two different statistical approaches to describing fluctuations are presented. The first approach uses correlation functions to quantify the fluctuations in the field amplitude and leads to a description of the average propagation of light intensity. In this description important effects like diffusion of light, localization and enhanced backscattering can be recognized. This theory is not new and is included as a theoretical background.

The second approach uses a probability density function to describe phase characteristics of the optical field. This leads to the notion of the weighted diffuse delay time, a quantity important for calculating the amount of energy stored in a slab of random material. This quantity also has a direct relation to the quantum mechanically interesting density of states. The statistical analysis of phase information is relatively new and a small correction to the existing theory [18] is suggested.

3.2 Correlation functions describing fluctuations

The first step in describing the fluctuations is to quantify the magnitude of the fluctuations. The average squared magnitude of the fluctuations at a certain point $\mathbf{r}$ and time t is called the variance,

$$\begin{aligned}\text{var}\,\Psi(\mathbf{r},t) &\equiv \left\langle |\Psi(\mathbf{r},t) - \langle\Psi(\mathbf{r},t)\rangle\,|^2 \right\rangle \\ &= \left\langle |\Psi(\mathbf{r},t)|^2 \right\rangle - \left\langle |\Psi(\mathbf{r},t)| \right\rangle^2 \\ &= \langle I(\mathbf{r},t)\rangle - \left\langle |\Psi(\mathbf{r},t)| \right\rangle^2, \end{aligned} \tag{3.1}$$

where the averaging operator $\langle\cdot\rangle$ denotes averaging over random realizations of the medium, as was explained in Chapter 2. This equation shows that the fluctuations have a direct relation to the physical concept of intensity. The second part of Eq.(3.1) was calculated in Chapter 2 and equals the absolute square of Eq. (2.21). In the following sections we will calculate the first part of Eq.3.1, which is the average intensity $\langle I\rangle$.

The time dependance of the average intensity will be studied in the frequency domain. According to the Wiener-Khinchin theorem the time dependent intensity can be written as a correlation function of the electrical field [25],

$$\langle I(\mathbf{r},\Omega)\rangle = \int d\omega \left\langle \Psi(\mathbf{r},\omega^-)\Psi^*(\mathbf{r},\omega^+)\right\rangle, \tag{3.2}$$

where $\omega^{\pm} = \omega \pm \Omega/2$. ω^+ and ω^- are the frequency components of the source. A stationary source only has a single frequency contribution, but a pulsed source has a certain bandwidth. Every pair of frequencies gives rise to a term $\Psi(\mathbf{r},\omega^-)e^{i\omega^- t}\Psi^*(\mathbf{r},\omega^+)e^{-i\omega^+ t} = \Psi(\mathbf{r},\omega^-)\Psi^*(\mathbf{r},\omega^+)e^{i\Omega t}$ in the intensity. In general, this bandwidth will be much smaller than the central frequency and therefore $\Omega \ll \omega$.

Eq. (2.3) is applied on both $\Psi(\mathbf{r},\omega^-)$ and $\Psi(\mathbf{r},\omega^+)$ in Eq. (3.2) in order to describe the fields as a function of the source field Ψ_s,

$$\langle I(\mathbf{r},\Omega)\rangle = \iiint d\omega d\mathbf{r}'_a d\mathbf{r}'_b R(\mathbf{r},\mathbf{r}'_a,\mathbf{r},\mathbf{r}'_b,\omega,\Omega)\Psi_s(\mathbf{r}'_a,\omega^-)\Psi_s^*(\mathbf{r}'_b,\omega^+), \tag{3.3}$$

where R is defined as the ensemble average of the product of the two field propagators,

$$R(\mathbf{r}_a,\mathbf{r}_b,\mathbf{r}'_a,\mathbf{r}'_b,\omega,\Omega) \equiv \left\langle G(\mathbf{r}_a,\mathbf{r}'_a,\omega^-)G^*(\mathbf{r}_b,\mathbf{r}'_b,\omega^+)\right\rangle. \tag{3.4}$$

R is recognized as a field-field correlation function. Since Eq. (3.3) is general and exact, it can be concluded that the correlation function, R, contains all information about the average intensity transport in a random medium. In the following section the correlation function will be analyzed and terms responsible for enhanced backscattering, localization and diffusion are identified.

It is possible to define higher order correlation functions, for example to describe fluctuations of the intensity (See [26] for a review on intensity correlations). In this thesis, higher order correlations will not be studied.

3.3 Diagrammatic representation of field correlations

In the previous section it was seen that the correlation function R has a direct relation to intensity propagation. R contains the sum of all possible paths between $\mathbf{r}'_a$ and $\mathbf{r}_a$ multiplied with all possible paths from $\mathbf{r}'_b$ to $\mathbf{r}_b$. Symbolically:

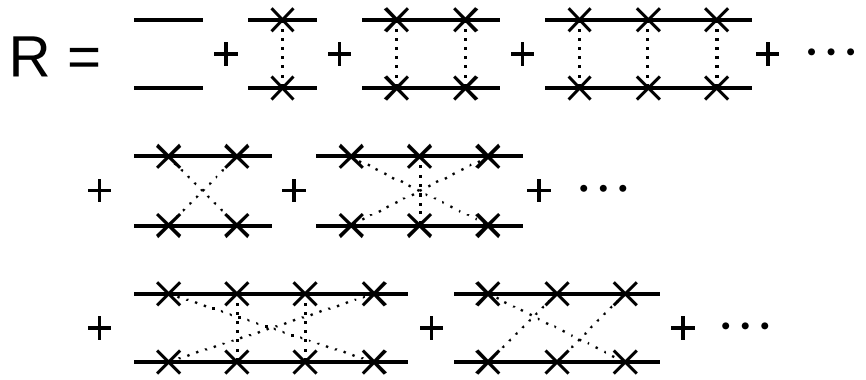

Figure 3.1: Diagrammatic expansion of correlation function $R = \langle GG^* \rangle$. Thick lines describe propagation without common scattering events. The crosses are the t-matrices of scatterers and the dotted lines indicate that the same scatterer occurs in both paths. Because of the independent scattering approximation, each scatterer appears only once in every path. The diagrams in the first row are the coherent propagation term $\langle G \rangle \langle G^* \rangle$ and the so called ladder terms. On second row the family of maximally crossed diagrams is shown and some of the many remaining diagrams are on the last line. The terms can be cascaded to create a new term in the diagram.

$$\begin{aligned} R &= \left\langle \sum_n G_{an} \sum_m G^*_{bm} \right\rangle \\ &= \langle G_{a1} G^*_{b1} \rangle + \langle G_{a1} G^*_{b2} \rangle + \langle G_{a2} G^*_{b1} \rangle + \langle G_{a2} G^*_{b2} \rangle + \dots \end{aligned} \tag{3.5}$$

R contains paths that have no scattering events in common and therefore are statistically independent, but there are also combinations of paths that do have common scatterers. These terms need special care in the averaging process. Figure 3.1 shows a diagrammatic expansion of R order by different types of diagrams. The upper lines correspond to the paths from $\mathbf{r}'_a$ to $\mathbf{r}_a$, the lower lines correspond to the paths from $\mathbf{r}'_b$ to $\mathbf{r}_b$. Crosses represent scatterers that need special treatment in the averaging process since they are present in both paths. Propagation is from the right to the left of the diagram and the common scatterers are connected by dotted lines so that is becomes clear in what order the scatterers occur in both paths.

The diagrams represent a two step averaging process, just as was used in Section 2.4. For every combination of paths the common scattering events are separated from the rest of the scattering and propagation. First a propagator for the average environment, not including the common scattering events, is calculated. This propagator is represented by the lines in the figure and is approximated by the average Green function $\langle G \rangle$. Secondly the contribution of the diagram to R is calculated for a given position of the common scatterers. Finally this contribution is averaged over all possible positions of the common scatterers.

Contributions to R can be divided in different classes of diagrams, including the coherent contribution, ladder diagrams, maximally crossed diagrams and a variety of other diagrams.

Coherent intensity propagation

The first term in Figure 3.1 belongs to paths that have no scatterers in common. Since the two paths are statistically independent, this term can be approximated by $\langle G \rangle \langle G^* \rangle$. As was seen in Chapter 2, the direction of coherent propagation is not affected by the medium. Therefore the direction of the corresponding coherent intensity propagation is determined by the source only.

The coherent contribution drops off very quickly with an extinction length ℓ. However, since the propagation direction is maintained, coherent intensity from a plane wave source can be dominant in this direction even after propagating over a few mean free paths. This is clearly seen from the experimental results that will be presented in Chapter 5.

Ladder diagrams

The ladder diagrams describe two paths visiting a series of common scatterers in the same order. The full Green functions that connect the common scattering events are equal for both paths, regardless of random realization. Consequently, if both paths have the same origin and the same destination ($\mathbf{r}'_a = \mathbf{r}'_b$ and $\mathbf{r}_a = \mathbf{r}_b$), the ladder terms always describe constructive interference and survive the ensemble averaging process.

In the ladder diagram description of light propagation, light intensity moves from one scatterer to another without being affected by interference. This is very similar to particles performing a random walk, which is the mechanism behind particle diffusion. One can therefore expect that the ladder terms are responsible for diffusion of light and on average describe light moving from areas with a high intensity towards areas with a low intensity. In the next section this is shown to be the case and a diffusion equation for light is formulated.

Maximally crossed diagrams

The maximally crossed diagrams are very similar to the ladder diagrams. They too describe two paths propagating along the same scatterers, but the direction of the paths is opposite. If both paths start and end at the same point, they have the same length and there will be constructive interference. These diagrams will survive ensemble averaging and on average describe light moving back to the origin.

The contribution of the maximally crossed diagrams to $R(\mathbf{r}, \mathbf{r}, \mathbf{r}, \mathbf{r})$ is equal to the contribution of the returning ladder diagrams. Therefore the amount of light intensity scattered back to a source is twice the amount that would be scattered back if only diffusion was occurring. This effect is called enhanced backscattering and has been experimentally demonstrated [4, 5, 7, 8].

The amount of light returning to the same scatterer by diffusive propagation is small if the mean free path is long. The returning maximally crossed diagrams have an equal contribution and can therefore be neglected in the limit of weak scattering. Alternatively, they can be expressed as a renormalization of the mean free path or the diffusion constant. This effect has been observed in samples with extremely strong scattering [15].

Maximally crossed diagrams that describe paths with a different start and end point do not always describe constructive interference. Their average contribution depends on

the mean free path and therefore these diagrams fall in the category of scale dependent diagrams which are treated below.

Scale dependent diagrams

Most diagrams do not always cause constructive or destructive interference. The upper path can be longer or shorter than the lower path, depending on the position of the common scatterers. The absolute value of the difference in travel time will determine wether the interference is constructive or destructive. We will call these diagrams 'scale dependent'.

The time it takes light to propagate along a certain path depends on the mean free path. Therefore, a longer mean free path means the distribution of travel times is wider.

If the spread in path length difference is much larger than the wavelength, the corresponding phase difference will have an almost uniform distribution between 0 and π and after ensemble averaging there will be no contribution to R. If the mean free path is very short, however, the path length difference will have a narrow distribution and certain phase differences will occur more often than others. It was predicted that for $k\ell = 2\pi\ell/\lambda \approx 1$ phase shifts around π are dominant [27], effectively canceling the ladder terms and inhibiting transport of intensity. This effect is called Anderson localization of light [1].

3.4 Diffusion

In the previous section it was explained that in weak scattering limit the ladder terms in the expansion of R are dominant. In this section, R will be approximated using only ladder terms and coherent propagation. It is shown that the intensity propagation described by the ladder terms corresponds to diffusion of light.

Approximation: *All diagrammatic contributions except ladder diagrams and coherent propagation will be neglected. This is a valid approximation if* $k\ell \gg 1$

3.4.1 The ladder equation

To calculate R with only ladder terms, a recursive approach is used. First R is separated in the sum of ladder terms L and the incoming and outgoing Green functions, as shown in Figure 3.2. $L(\mathbf{r}, \mathbf{r}_b, \mathbf{r}', \mathbf{r}'_b) = L(\mathbf{r} - \mathbf{r}')\delta(\mathbf{r} - \mathbf{r}_b)\delta(\mathbf{r}' - \mathbf{r}'_b)$ is called the ladder propagator and is the sum of all ladder terms starting at a scatterer in $\mathbf{r}'$ and ending at a scatterer in $\mathbf{r}$ in a uniform medium. A recursive definition of $L(\mathbf{r} - \mathbf{r}')$ is found from the last diagram in Figure 3.2.

In words, this diagram means that intensity propagation from a scatterer in $\mathbf{r}'$ to a scatterer in $\mathbf{r}$ is composed of two parts. The first part is just scattering at a single scatterer when $\mathbf{r}$ equals $\mathbf{r}'$. The second part corresponds to propagating from the starting scatterer $\mathbf{r}'$ to a second last scatterer $\mathbf{r}_1$ (this propagation is described by L), then propagating without common scattering events (the two lines) and finally scattering on the last scatterer. After

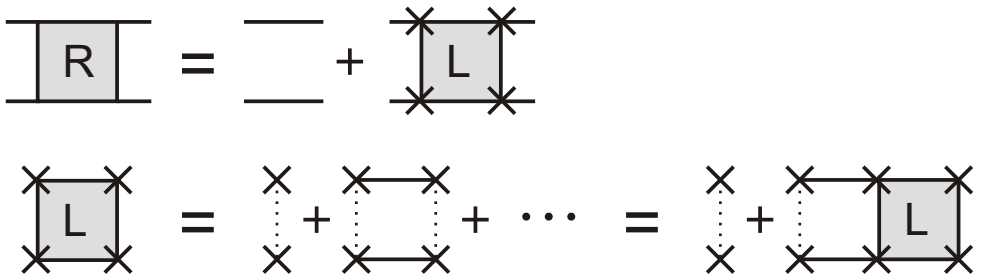

Figure 3.2: Correlation function R is approximated by the coherent contribution and the ladder propagator L. This propagator is a summation of all ladder terms and can be defined in a recursive way. The approximation is valid for $k\ell \gg 1$

averaging over the position of scatterer $\mathbf{r}_1$, just as was done in Chapter 2, the recursive ladder equation can be written,

$$L(\mathbf{r}-\mathbf{r}',\omega,\Omega) = nt(\omega^-)t^*(\omega^+)\delta(\mathbf{r}-\mathbf{r}')+nt(\omega^-)t^*(\omega^+)\int d\mathbf{r}_1 F(\mathbf{r}-\mathbf{r}_1,\omega,\Omega)L(\mathbf{r}_1-\mathbf{r}',\omega,\Omega), \tag{3.6}$$

where $F(\mathbf{r},\omega,\Omega) \equiv \langle G(\mathbf{r},\omega^-)\rangle \langle G^*(\mathbf{r},\omega^+)\rangle$. This equation can be solved in wavevector space,

$$\begin{aligned} L(\mathbf{P},\omega,\Omega) &= nt(\omega^-)t^*(\omega^+)\left[1+F(\mathbf{P},\omega,\Omega)L(\mathbf{P},\omega,\Omega)\right] \\ &= \frac{1}{\left[nt(\omega^-)t^*(\omega^+)\right]^{-1} - F(\mathbf{P},\omega,\Omega)}. \end{aligned} \tag{3.7}$$

$F(\mathbf{P},\omega,\Omega)$ can be found using the result found in Chapter 2, $\langle G(\mathbf{r},\omega)\rangle = e^{iK(\omega)\mathbf{r}}/(4\pi r)$ where $K \equiv kn_{\text{eff}} + i/(2\ell)$, and performing a Fourier transform,

$$F(\mathbf{P},\omega,\Omega) = \frac{i}{8\pi P}\ln\left(\frac{\Delta K + P}{\Delta K - P}\right), \tag{3.8}$$

where $\Delta K \equiv K^*(\omega^+) - K(\omega^-)$. Although this result yields an expression for the ladder propagator, it is hard to conclude anything from this form. To simplify things, we focus at the slow, long distance behavior of L. Slow means we look at frequencies much lower than the optical frequency, $\Omega \ll \omega$. Long distance means the distances are long compared to the mean free path, $1/P \gg \ell \approx |1/\Delta K|$. A direct Taylor expansion of L is not possible, since the expansion in P diverges as Ω becomes small and vice versa. Therefore the reciprocal of L is expanded. First F is expanded to second order P,

$$F(\mathbf{P},\omega,\Omega) = \frac{i}{8\pi P}\left[\ln(1+\frac{P}{\Delta K}) - \ln(1-\frac{P}{\Delta K})\right] \tag{3.9}$$

$$\approx \frac{i}{8\pi}\left[\frac{2}{\Delta K} + \frac{2P^2}{3\Delta K^3}\right], \tag{3.10}$$

From the definition of ΔK it follows that $d\Delta K/d\Omega = \mathrm{Re}\{dK/d\omega\} \equiv 1/v_{\mathrm{gr}}$, where v_{gr} is the group velocity in the random medium. Expanding to first order in Ω gives,

$$F(\mathbf{P},\omega,\Omega) \approx \frac{i}{4\pi}\left[\frac{1}{\Delta K(0)} - \Omega\frac{1/v_{\mathrm{gr}}}{\Delta K^2(0)} + \frac{P^2}{3\Delta K^3(0)}\right] \tag{3.11}$$

$$= \frac{\ell}{4\pi}\left[1 - i\Omega\frac{\ell}{v_{\mathrm{gr}}} - \frac{P^2\ell^2}{3}\right], \tag{3.12}$$

where terms of order $P^2\Omega$ and higher were neglected and $\Delta K(0) = i/\ell$ was used in the last step. All needs to be expanded now is the first part of the denominator in Eq.(3.7),

$$\frac{1}{nt(\omega^-)t^*(\omega^+)} \approx \frac{1}{nt(\omega)t^*(\omega)} - \Omega\frac{t\frac{dt^*}{d\omega} - \frac{dt}{d\omega}t^*}{2n\left[t(\omega)t^*(\omega)\right]^2}$$

$$= \frac{\ell}{4\pi}\left[1 + i\Omega\mathrm{Im}\left\{\frac{d\ln t}{d\omega}\right\}\right], \tag{3.13}$$

where it was used that in absence of absorption, $nt(\omega)t^*(\omega) = 4\pi/\ell$. This is called the optical theorem, which is a condition on the t-matrix to enforce energy conservation. Substituting Eqs. (3.12) and (3.13) into (3.7), we finally find

$$L(\mathbf{P},\omega,\Omega) = \frac{4\pi}{\ell}\left[\frac{i\Omega\ell}{v_e} + \frac{P^2\ell^2}{3}\right]^{-1}, \tag{3.14}$$

where the energy velocity v_e is defined $\ell/v_e \equiv \ell/v_{\mathrm{gr}} + \mathrm{Im}\{d\ln t/d\omega\}$*. We now have found a simple expression for the ladder propagator, describing propagation of intensity from one scatterer to another. The correlation function $R(r,r,r',r')$ can be found easily in the wavevector domain by reconnecting incoming and outgoing Green functions and adding the coherent contribution,

$$R(\mathbf{P},\omega,\Omega) = F(\mathbf{P},\omega,\Omega) + F(\mathbf{P},\omega,\Omega)L(\mathbf{P},\omega,\Omega)F(\mathbf{P},\omega,\Omega) \tag{3.15}$$

$$= \frac{1}{nt(\omega^-)t^*(\omega^+)}L(\mathbf{P},\omega,\Omega), \tag{3.16}$$

where equation (3.7) was used in the last step. Now the dynamics of the intensity coming from a point source can be found,

$$\langle I(\mathbf{P},\Omega)\rangle = \int d\omega R(\mathbf{P},\omega,\Omega)\Psi_s(\omega^-)\Psi_s^*(\omega^+) \tag{3.17}$$

$$\approx R(\mathbf{P},\omega_0,\Omega)I_s(\Omega), \tag{3.18}$$

*The first term on the right hand side is the time it takes for a coherent pulse to travel a mean free path and could therefore be called travel time. The second part represents a time completely depending on the t-matrix and corresponds to dwelling at the scatterer. In literature [22], however, the term travel time is defined ℓ/c and the coherent scattering delay is part of the dwell time.

R acts as the propagator of the intensity. If the source has a limited bandwidth around ω_0, R can be assumed to be independent of ω and the second line of Eq. (3.18) can be used. In the time domain we find:

$$I(\mathbf{P},t) = \int d\tau R(\mathbf{P},\tau) I_s(t-\tau), \tag{3.19}$$

with

$$R(\mathbf{P},t) = \frac{2\pi^2}{\ell^2} D e^{-P^2 D t} \Theta(t), \tag{3.20}$$

where $D \equiv v_E \ell/3$ is the diffusion constant and $\Theta(t)$ is the Heaviside step function. This equation describes diffusive propagation of light. Any inhomogeneous distribution of the intensity (components with $\mathbf{P} \neq 0$) will decay to zero. This process is faster for high frequency components, corresponding to short distances, and faster if the diffusion constant is larger. Eventually the intensity will be spread uniformly.

In real space the intensity propagator reads,

$$R(\mathbf{r},t) = \frac{v_E}{\ell(4Dt)^{(3/2)}} e^{-r^2/(4Dt)} \tag{3.21}$$

Finally, a well known form of the diffusion equation is found from (3.20) by taking the derivatives,

$$\frac{\partial R(\mathbf{r},t)}{\partial t} = D\nabla^2 R(\mathbf{r},t). \tag{3.22}$$

3.4.2 Diffusion in a slab geometry

In an experiment we will never have an infinite medium and surface effects have to be taken into account. To calculate how the light intensity is distributed in a slab of disordered material, boundary conditions have to be imposed. The derivation of these boundary conditions and an analysis of the propagation of light through a finite slab of material can be found in Appendix 3.4.2.

The model of diffusion through a slab with simplified boundary conditions is shown in Figure 3.3. The boundary conditions take the form of extrapolation lengths z_{e1} and z_{e2}. The diffuse intensity inside the slab is described in terms of sinusoidal eigenmodes that are zero at $-z_{e1}$ and at $L + z_{e2}$. This is a mathematical construction and of course does not give meaningful results outside the slab of diffuse material ($z < 0$ or $z > L$). Since the eigenmodes are sinusoidal, Eq. (3.20) can be used to calculate the dynamic behavior of these modes.

A different complication is that light entering the sample is not immediately diffuse; on average it takes one mean free path for the incoming light to become diffuse, so the external source of coherent light is modeled as an internal source of diffuse light at $z = \ell$. Finally, in some models [23, 28, 9] the outgoing flux is evaluated at a distance z_{ej} from the surface to compensate for the diffusion equation not being valid close to the surface.

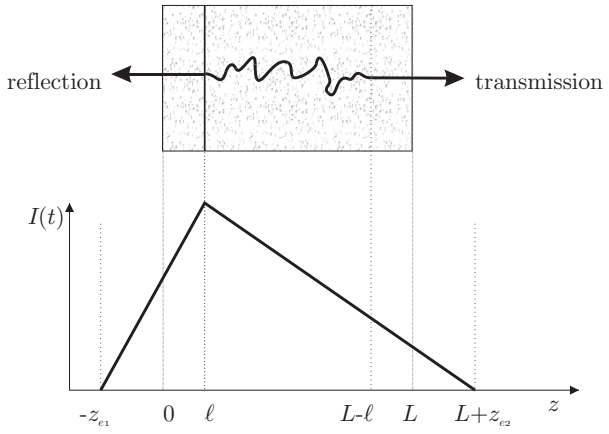

Figure 3.3: Model of diffusion in a slab. The simplified boundary conditions are $I(-z_{e1}) = 0$, $I(L + z_{e2}) = 0$. The source is approximated by a plane source at depth ℓ (figure above). The steady state intensity is given in the figure below.

This model gives an equation for the intensity flux transmitted through a sample, J_T, for a source $J_s = \delta(t)$,

$$J_T(t) = \frac{\pi D}{L'} \sum_{n=1}^{\infty} n \exp\left(\frac{-\pi^2 n^2 Dt}{L'^2}\right) \cos\left(\pi n \frac{L' - z_{\mathrm{ej}} - z_{e_2}}{L'}\right) \sin\left(\pi n \frac{\ell + z_{e_2}}{L'}\right) \Theta(t), \quad (3.23)$$

The long time behavior of the transmitted intensity is found by taking only the $n = 1$ term and is seen to be an exponential decay with a factor $\pi^2 D/L'^2$. This value is of particular interest, since it can be derived easily from measurements and yields the diffusion constant. The steady state solution can be found more easily by solving the diffusion equation (3.22) with the corresponding boundary conditions directly. The solution for the simplified boundary conditions is a triangle (see Figure 3.3).

An important value that can be calculated using equation (3.23) is the static transmission coefficient, T, expressing what part of the incoming light is transmitted (in any direction),

$$T = \frac{\ell + z_{e1}}{L'}. \quad (3.24)$$

A second parameter of importance is the diffuse travel time $\tau_d \equiv \left\langle \int dt J_T t \right\rangle / \left\langle \int dt J_T \right\rangle$. This value expresses the average time it takes light to travel through the disordered slab,

$$\tau_d = \frac{L'^2}{6D} - \tau_e, \quad (3.25)$$

τ_e is the correction for edge effects,

$$\tau_e = \frac{L'^2}{6D} - \frac{z_{\ell 1}^2 + 3 z_{\ell 2}^2}{6D}, \quad (3.26)$$

where $z_{\ell 1} \equiv z_{e1} + \ell$ and $z_{\ell 1} \equiv z_{e1} + z_{\mathrm{ej}}$. This means that the diffuse traversal time depends on the ejection depth z_{ej}. It is not certain if this value should be zero or a fraction of the mean free path; a sensitive measurement of τ_e can solve this question.

3.5 Probability distributions describing fluctuations

In the previous section the fluctuations in the amplitude of the electrical field were described using a correlation function. A different technique to describe fluctuations is to use a joint probability function. A probability function does not only describe the average value and the variance, but it gives a full mapping of possible values and their corresponding probabilities. In this section an approximate probability distribution of the electrical field will be used to calculate probability distributions of intensity, travel time, and density of states. This technique is very powerful since it can describe both phase fluctuations and intensity fluctuations and yields a probability function instead of just a mean value.

A joint probability function describes what the chance is to find certain values of electrical field complex amplitudes, $\Psi_1, \ldots, \Psi_N$, when measuring the fields at N different positions and/or frequencies.

It is only possible to construct the probability function from correlation functions if the correlation functions are known up to infinite order. This corresponds to knowing all moments of the fluctuations. The first moment $\langle \delta\Psi \rangle$ is zero. The second moment $\langle \delta\Psi \delta\Psi^* \rangle$ is the variance and was calculated in the previous section. The third moment is zero for symmetry reasons. Calculating the fourth moment is possible, but this will not be done here (for calculations of the intensity-intensity correlation see for example [26, 29]).

If the fourth and higher moments of the fluctuations in the electrical field are neglected, all correlation functions can be constructed from the first order correlation function R and the field average. This approximation is called the C_1 approximation and allows the joint probability function to be written. The notation $\mathbf{\Psi} \equiv (\Psi_1 - \langle \Psi_1 \rangle, \Psi_2 - \langle \Psi_2 \rangle, \ldots, \Psi_N - \langle \Psi_N \rangle)$ is introduced, defining a vector of length N, containing the fluctuations measured for N different combinations of position and frequency.

$$P(\mathbf{\Psi}) = \frac{1}{\pi^N \det C} \exp\left(-\mathbf{\Psi}^{*T} C^{-1} \mathbf{\Psi}\right) \tag{3.27}$$

Here $\mathbf{\Psi}^T$ denotes the transposed vector and C is the first order correlation matrix, $C_{ij} \equiv \left\langle \Psi_i \Psi_j^* \right\rangle$. For $N = 1$, Eq. (3.27) describes a single Gaussian distribution. For higher values of N it describes N Gaussian distributions that are cross correlated as quantified by C.

Approximation: *Higher order correlations are neglected; a Gaussian distribution of the field amplitudes is assumed. This choice for a Gaussian distribution corresponds to the assumption that a large number of propagation paths contribute to the field. According to the law of large numbers the corresponding probability distribution is Gaussian if these paths are independent [30].*

Approximation: *The coherent contribution $\langle \Psi \rangle$ is neglected, therefore the complex amplitudes of the fields have a Gaussian distribution with zero mean. This approximation is*

valid for samples thicker than a few mean free paths.

In a finite system, light entering or exiting a random material can be decomposed in a finite number of orthogonal modes. A combination of an incoming and an outgoing mode is called a channel. In the following sections statistics of single channel transmission is investigated. This means that the amplitudes $\Phi_1, \ldots, \Phi_N$ of outgoing light belong to the same mode, but correspond to different frequencies.

3.5.1 Speckle intensity distribution

The simplest form of the probability density function (3.27) is for a single channel and a single frequency. Substituting $N = 1$ and using the average intensity, $\langle \Psi \Psi^* \rangle = \langle I \rangle$, gives,

$$P(\Psi) = \frac{1}{\pi \langle I \rangle} \exp\left(\frac{-\Psi^* \Psi}{\langle I \rangle}\right) \tag{3.28}$$

We change variables from the complex Ψ to polar coordinates (A, ϕ), where $\Psi = Ae^{i\phi}$. Since P is a probability density function a change of variables introduces a factor equal to the Jacobian of the coordinate transform [30]. In this case a factor A is introduced. Since the resulting expression does not depend on ϕ, the phase can be integrated out,

$$P(A) = \frac{2A}{\langle I \rangle} \exp\left(\frac{-A^2}{\langle I \rangle}\right) \tag{3.29}$$

Finally substituting $I = A^2$ introduces the Jacobian $\partial A / \partial I = 1/(2\sqrt{I}) = 1/(2A)$ and yields,

$$P(I) = \frac{1}{\langle I \rangle} \exp\left(\frac{-I}{\langle I \rangle}\right), \tag{3.30}$$

which is the well known Rayleigh distribution.

3.5.2 Diffuse delay time

In Section A.3 an expression for the diffuse traversal time, i.e. the average time it takes an incoherent pulse to travel through a slab of random material, was found. In this section a single channel delay time will be defined, which describes how long light travels through a single channel in a random medium before it is transmitted or reflected. Using the assumption of Gaussian statistics, a probability distribution for this delay time is calculated. We will find that the average delay time in transmission equals the diffuse traversal time that was found before. Furthermore is is shown that the single channel delay time has the possibility of being negative.

The single channel delay time ϕ' is defined as the derivative of the phase of the transmitted light with respect to the angular frequency. To evaluate this derivative, the joint probability function for two fields at two frequencies close to each other is calculated. The probability of finding a certain phase difference can be calculated from this function. In the limit of zero frequency difference, this function gives the delay time distribution.

$$\phi' \equiv \frac{d \arg \Psi(\omega)}{d\omega} = \lim_{(\omega_1-\omega_2)\to 0} \frac{\arg \Psi(\omega_1) - \arg \Psi(\omega_2)}{\omega_1 - \omega_2} \tag{3.31}$$

The joint probability function (3.27) is written for two fields. The indices will be used to indicate different frequencies, so $\Psi_{1,2} = \Psi(\omega_{1,2})$. In the correlation matrix $\langle \Psi_1 \Psi_2^* \rangle$ is written $C(\Omega)$, where $\Omega \equiv \omega_1 - \omega_2$. The intensities are normalized to have: $\langle \Psi_i \Psi_i^* \rangle = 1$ for all i. From the definition, $C(-\Omega) = C^*(\Omega)$, which is used to complete the correlation matrix,

$$C = \begin{pmatrix} 1 & C(\Omega) \\ C^*(\Omega) & 1 \end{pmatrix}; \qquad C^{-1} = \frac{1}{\det C} \begin{pmatrix} 1 & -C(\Omega) \\ -C^*(\Omega) & 1 \end{pmatrix}, \tag{3.32}$$

$$P(\Psi_1, \Psi_2) = \frac{1}{\pi^2 \det C} \exp\left(-\frac{|\Psi_1|^2 + |\Psi_2|^2 - \Psi_1^* \Psi_2 C(\Omega) - \Psi_2^* \Psi_1 C^*(\Omega)}{\det C} \right). \tag{3.33}$$

Some substitutions are made to introduce the phase of Ψ explicitly. $\Psi_{1,2} \Rightarrow A_{1,2} e^{i\phi_{1,2}}$ and $C(\Omega) \Rightarrow A_c e^{i\phi_c}$. The first two substitutions affect the parameters of the probability function and introduce extra factors of A_1 and A_2.

$$P(A_1, A_2, \phi_1, \phi_2) = \frac{A_1 A_2}{\pi^2 \det C} \exp\left(-\frac{A_1^2 + A_2^2 - 2A_1 A_2 A_c \cos(\phi_1 - \phi_2 - \phi_c)}{\det C} \right). \tag{3.34}$$

Substituting $\phi_1 - \phi_2 \Rightarrow \phi'\Omega$, one of the phases can be integrated out. Two further substitutions are made $I = A_1^2$ and $R = (A_2/A_1 - 1)/\Omega$. R and ϕ' are the only two statistical parameters that depend on Ω. In the limit $\Omega \to 0$, the latter will be the phase derivative that we are interested in.

$$P(I, R, \phi') = \frac{I\Omega^2(1 + R\Omega)}{\pi(\det C)} \exp\left(-I \frac{1 + (1 + R\Omega)^2 - 2(1 + R\Omega) A_c \cos(\phi'\Omega - \phi_c)}{\det C} \right). \tag{3.35}$$

Since we are interested in the probability distribution belonging to an infinitely small Ω, it is permitted to expand Eq. (3.35) in Ω. For the expansion of the correlation function the property $C(-\Omega) = C^*(\Omega)$ is used. Together with $C(0) = 1$, this implies that the expansion of the correlation function is $C(\Omega) = 1 + ia\Omega + b\Omega^2 + O(\Omega^3)$. Because $|C|$ has to be lower than or equal to one, b must be negative. In Appendix 3.4.2 this expansion is calculated for light transmitted through a slab of random material. From this derivation it can be learned that a is a time and in transmission equals the diffuse traversal time $\tau_d \equiv \langle \int dt J_T t \rangle / \langle \int dt J_T \rangle$. Instead of b, a dimensionless parameter $Q \equiv -2b/a^2 - 1$ is used to simplify the notation.

All variables in Eq. (3.35) that depend on the correlation function can now be written in terms of a and Q.

$$\phi_c = a\Omega + O(\Omega^3), \tag{3.36a}$$
$$\det C = Qa^2\Omega^2 + O(\Omega^3), \tag{3.36b}$$
$$A_c = 1 - \frac{1}{2}Qa^2\Omega^2 + O(\Omega^3), \tag{3.36c}$$

The parameters Q and a can be calculated for transmission and reflection of a slab geometry. For transmission we find (See Appendix 3.4.2):

$$a_T = \tau_d = \frac{L'^2}{6D} - \frac{z_{\ell 1}^2 + 3z_{\ell 2}^2}{6D}, \tag{3.37}$$
$$Q_T = \frac{2}{5} - \frac{z_{\ell 1}^4 + 12z_{\ell 2}^4 + 3z_{\ell 1}^2 z_{\ell 2}^2 - (z_{\ell 1}^2 + 3z_{\ell 2}^2)(L')^2}{45D^2\tau_d^2}, \tag{3.38}$$

where $z_{\ell 1} \equiv z_{e1} + \ell$ and $z_{\ell 1} \equiv z_{e1} + z_{\rm ej}$. For very thick slabs ($L \gg \ell, z_{e1}, z_{e2}$) edge effects can be neglected and we find $a_T = L^2/(6D)$ and $Q_T = \frac{2}{5}$, which correspond to the values in [18]. For this case absorption was calculated to have no effect on a and cause Q_T to become smaller [18],

$$Q_T = \frac{X^2 - 2\sinh X + \frac{1}{2}X\sinh 2X}{(X\cosh X - \sinh X)^2}, \tag{3.39}$$

where X equals the sample thickness L divided by the absorption length L_a. In reflection different values for Q and a are found and the energy velocity can be extracted from the measurements [21],

$$Q_R = \frac{2}{5}\frac{L + z_{e1} + z_{e2}}{\ell + z_{e1}}, \tag{3.40}$$
$$a_R = \frac{4}{3}\frac{L + z_{e1} + z_{e2}}{3v_E}, \tag{3.41}$$

Using expansions (3.36a-3.36c) in Eq. (3.35), the probability function can be written in terms of these parameters. After expanding the cosine to second order in Ω, we find an expression for P in the limit $\Omega \to 0$,

$$\begin{aligned} P(I, R, \phi') &= \frac{I\Omega^2(1 + R\Omega)}{\pi Qa^2\Omega^2} \exp\left(-I\frac{R^2\Omega^2 + Qa^2\Omega^2 + (\phi' - a)^2\Omega^2}{Qa^2\Omega^2} + O(\Omega^3)\right) \\ &= \frac{I}{\pi Qa^2} \exp\left(-I\frac{R^2 + (\phi' - a)^2}{Qa^2} - I\right) + O(\Omega). \end{aligned} \tag{3.42}$$

The integration over R can be performed now,

$$P(I, \phi') = \sqrt{\frac{I}{\pi Qa^2}} \exp\left(-\frac{I(\phi' - a)^2}{Qa^2} - I\right). \tag{3.43}$$

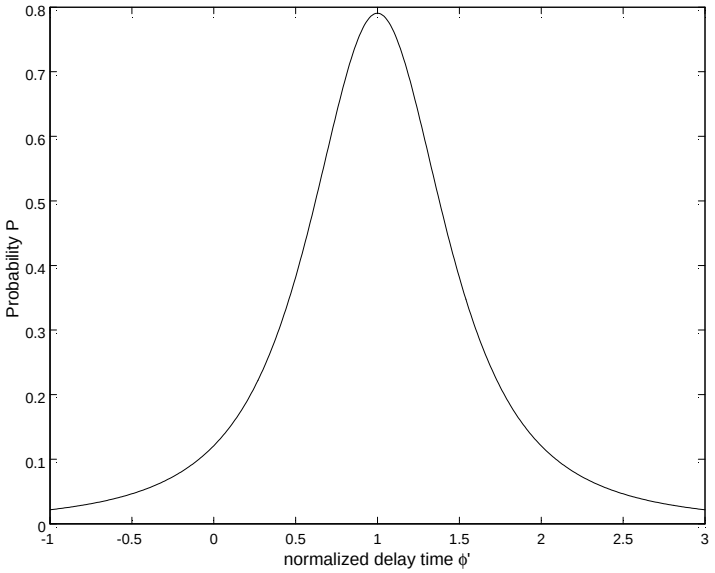

Figure 3.4: Probability distribution of the diffuse delay time. The delay time is normalized to the average delay time. It can be seen that negative delay times are possible but not very likely.

Using $\int_0^\infty dI\sqrt{I}\exp(-\alpha I) = \sqrt{\pi}/2\alpha^{3/2}$ with $\alpha = (\phi' - a)^2/Qa^2 + 1$, we finally find the desired probability distribution,

$$P(\phi') = \frac{Qa^2}{2\left[(\phi' - a)^2 + Qa^2\right]^{(3/2)}}. \tag{3.44}$$

Since this probability function is symmetrical around $\phi' = a$, this will be the expectation value of phase derivative. The normalized phase derivative $\hat{\phi}' \equiv \phi'/\langle\phi'\rangle$ is introduced to obtain a probability function that only depends on the dimensionless parameter Q [18].

$$P(\hat{\phi}') = \frac{Q}{2\left[(\hat{\phi}' - 1)^2 + Q\right]^{(3/2)}}. \tag{3.45}$$

A plot of this probability distribution is given in Figure 3.4. In Section 5.2 measurements of the probability function will be presented. In transmission without absorption and edge effects, $Q = 0.4$, but in reflection the mean free path, the extrapolation length and the sample thickness influence this parameter. In reflection the energy velocity can be found from the average value of ϕ'.

From Eqs. (3.44) and (3.45) it can be seen that the delay time can be negative. The probability for the delay time to be lower than zero can be used as a calibration point for measurements. Integration gives $P(\phi' < 0) = P(\hat{\phi}' < 0) = 1/2 - 1/(2\sqrt{1+Q})$, which for transmission without absorption is approximately 7.7%

3.5.3 Density of states and weighted delay time

Another interesting parameter is the weighted delay time $W_{ab} \equiv I_{ab}\phi'_{ab}$. This quantity consists of an intensity and a time and it is proportional to the amount of electromagnetic

energy in channel ab. An important property of W is that the sum of W over all channels gives the number of states per frequency interval $d\omega$.

$$N(\omega) = \frac{1}{\pi} \sum_{a,b}^{2M} I_{ab}\phi'_{ab} \tag{3.46}$$

This density of states (DOS) is an important quantity in quantum mechanics and determines the radiative decay rates of exited atoms or molecules. In this section the probability distribution of W will be calculated using the same technique as was used to calculate $P(\phi')$ in the previous section.

Equation (3.43) is taken as a starting point and $W = I\phi'$ is substituted for ϕ'.

$$P(W, I) = \sqrt{\frac{1}{\pi I Q a^2}} \exp\left(-\frac{I(W/I - a)^2}{Qa^2} - I\right) \tag{3.47}$$

Integrating over I gives:

$$P(W) = \frac{1}{a\sqrt{1+Q}} \exp\left(\frac{-2|W|}{(\operatorname{sgn} W + \sqrt{1+Q})a}\right) \tag{3.48}$$

Where $\operatorname{sgn} W = -1$ for $W < 0$ and $\operatorname{sgn} W = 1$ for $W > 0$. The expectation value of W can be found by calculating the integral $\int dW P(W)W$ and evaluates to $\langle W \rangle = a = \tau_d$. A different derivation of this relation can be found in [19]. Now the probability function can be written in terms of the normalized weighted delay time $\hat{W} \equiv W/\langle W \rangle$[†],

$$P(\hat{W}) = \frac{1}{\sqrt{1+Q}} \exp\left(\frac{-2|\hat{W}|}{\operatorname{sgn} \hat{W} + \sqrt{1+Q}}\right) \tag{3.49}$$

This probability function is plotted in Figure 3.5. From this equation it can be concluded that negative weighted delay times are possible, but less likely than positive values. The normalized probability function is only a function of the dimensionless Q and thus gives a different way of measuring this parameter. Measurements of $P(W)$ are presented in Section 5.2.

3.6 Summary

It was shown that the field correlation function in a random medium describes intensity propagation. The correlation function was expanded diagrammatically in coherent propagation, diffusion, enhanced backscattering and various interference terms. The terms contributing to coherent propagation and diffusion were calculated and the diffusion equation for light was found.

The diffusion equation was applied to a slab geometry and the diffuse traversal time was calculated. This value was seen to depend on the ejection depth, a parameter describing from what depth light leaves the sample. Different values for the ejection depth are used

[†]The equation used in [18] erroneously contains the Heaviside step function instead of the signum function.

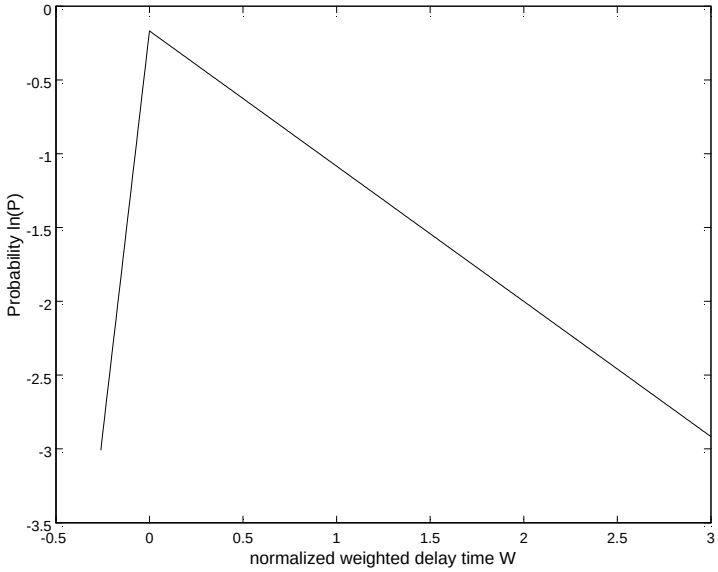

Figure 3.5: Probability distribution of the weighted delay time. This value is normalized to the average delay time. It can be seen that negative weighted delay times are very unlikely.

in literature and an accurate measurement of the diffuse traversal time should be able to tell what is the right value.

A complementary approach used joint probability functions to describe the fluctuations of the field and takes into account the phase of the field. This method was used to calculate the probability distributions of the delay time and the weighted delay time.

The result of the theoretical elaborations is a number of predictions that can be tested experimentally. Especially the diffuse traversal time is interesting, since it can be extracted from intensity measurements (Eq. 3.25) and from the phase statistics (Eqs. 3.44 and 3.48). In the following chapter the setup used to perform these experiments will be described. The measured time resolved diffusion, the diffuse delay time distribution and the weighted delay time distribution will be presented in Chapter 5.

Chapter 4

Time resolved pulse interferometry

4.1 Introduction

In the previous two chapters a theoretical model for the propagation of light in random media was presented. To test this theory experimentally we would like to be able to extract as much information from the sample as possible. The ideal situation is where an arbitrary field pattern can be launched into the medium at any desired frequency and where the whole field distribution can be measured.

In practice we are limited to certain modes and frequencies for inserting the light and we can only measure light leaving the sample. A different problem is that optical detectors measure light intensity and cannot measure the phase of the field directly. Even the relatively slow dynamics of diffusion is hard to measure since for the samples that are used time scales are in the picosecond range.

To exceed the limitations of standard detection techniques, a method was developed that allows an extremely high resolution time resolved measurement [13]. This method uses interfering pulses to measure the complex transfer function of a sample for a whole frequency range simultaneously and can resolve the oscillations of the electrical field. Because of this, it provides far more information than stationary intensity measurements give. The setup that was used in the experiments is based on the one described in [13] but has been improved to facilitate alignment and allow reflection measurements.

4.2 Working principle

Time resolved pulse interferometry makes use of two base principles. The first principle is that although the oscillation period of the electrical field is extremely short, it is relatively easy to generate a delay that is a fraction of this time. This can be done by changing the length of the propagation path. A length difference of a single wavelength corresponds to a time delay of a single period. In this experiment a wavelength of 775 nm was used and it is possible to regulate the length of the propagation path to within fractions of this distance.

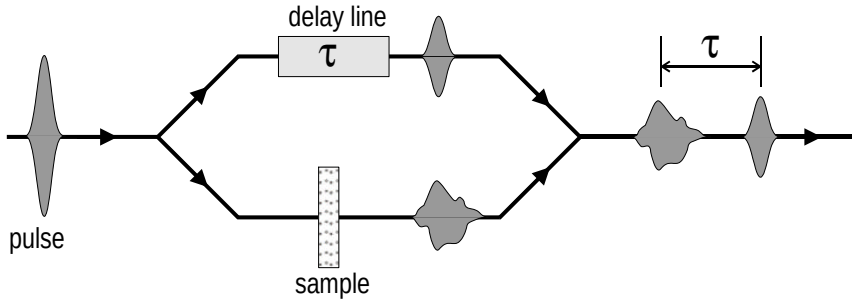

Figure 4.1: Schematic representation of the pulse interferometry method. A pulse of light propagates through the sample and interferes with an undisturbed reference pulse that has a variable delay time τ. By scanning this delay and making a reference measurement without a sample, the transfer function of the sample can be reconstructed.

The second principle of interferometry measurements is that an optical detector detects the intensity of the light, which is the square of the field amplitude. When two superimposed electrical fields reach a detector the measured intensity contains cross terms of both fields,

$$I(t) = |E_1(t) + E_1(t)|^2 \tag{4.1}$$
$$= |E_1(t)|^2 + |E_2(t)|^2 + E_1(t)E_2^*(t) + E_1^*(t)E_2(t) \tag{4.2}$$

In time resolved pulse interferometry, one of the pulses is a reference pulse E_r and the other pulse has traveled through the sample and is called the signal pulse E_s. The reference pulse is delayed for a certain amount τ. A simple setup for doing this is shown in Figure 4.1. In this setup the pulses are repeated with a certain period T_{pulse} and the measured intensity is integrated over many of such periods $T_m \gg T_{\text{pulse}}$. As a result, the detector signal now only depends on the pulse shapes and the delay τ,

$$I(\tau) = \frac{1}{T_m}\int_{-T_m/2}^{T_m/2} dt|E_s(t)|^2 + |E_r(t)|^2 + [E_s(t)E_r^*(t+\tau) + c.c.]\,. \tag{4.3}$$

The part that does not depend on τ is denoted by I_0, the average intensity. Substituting the Fourier representations of the signal and reference pulse-shapes gives an important result in the limit $T_m \to \infty$

$$I(\tau) = I_0 + \frac{1}{T_m}\int_{-T_m/2}^{T_m/2} dt \iint d\omega_1 d\omega_2 \left[E_s(\omega_1)e^{i\omega_1 t}E_r^*(\omega_2)e^{-i\omega_2(t+\tau)} + c.c.\right]$$
$$= I_0 + \int d\omega \left[E_s(\omega)E_r^*(\omega)e^{-i\omega\tau} + c.c.\right] \tag{4.4}$$

The function $I(\tau)$ is called the interferogram. By removing offset I_0 and performing a Fourier transform, information about the signal pulse can be extracted from the interferogram,

$$I(\omega') = \int d\tau \int d\omega \left[E_s(\omega)E_r^*(\omega)e^{-i\omega\tau} + E_s^*(\omega)E_r(\omega)e^{i\omega\tau}\right] e^{-i\omega'\tau}$$
$$= \begin{cases} E_s^*(\omega')E_r(\omega') & \omega' > 0 \\ 0 & \omega' = 0 \\ E_s(-\omega')E_r^*(-\omega') & \omega' < 0, \end{cases} \tag{4.5}$$

where it was used that the pulses only contain positive (i.e. forwardly propagating) frequencies. As can be seen from this equation, the signal pulse can be reconstructed from the negative frequencies in the interferogram if the reference signal is known.

Most of the time we are more interested in the transfer function of the sample than in the response to a certain input. The transfer function equals the field propagator from one side of the sample to the other side, $H(\omega) \equiv G(\mathbf{r}_{\text{out}}, \mathbf{r}_{\text{in}}, \omega)$, taking into account boundary effects. This transfer function can be found by comparing the situation without sample ($E_s = H_{\text{air}}E_{s0}$) to the situation with sample ($E_s = H_{\text{sample}}E_{s0}$) for positive frequencies*,

$$H_{\text{sample}}(\omega) = \frac{H_{\text{sample}}(\omega)E_{s0}(\omega)E_r^*(\omega)}{E_{s0}(\omega)E_r^*(\omega)} = \frac{I_{\text{sample}}(-\omega)}{I_{\text{air}}(-\omega)}H_{\text{air}}(\omega). \tag{4.6}$$

Since the transfer function of a slab of air with thickness L is known to be $H_{\text{air}}(\omega) = e^{i\omega L/c}$, the transfer function of the sample can be calculated now. From this function the intensity transfer and the diffuse delay time can be calculated, allowing an experimental test of the theory developed in the previous chapters.

4.3 Setup

The most difficult part of the pulse interferometry technique is scanning the delay time. Scanning the mirror or retroreflector of the delay line has to be done with a sub-wavelength precision while keeping the bundles of both paths aligned. Most importantly this has to be done without causing vibrations that would destroy the interference pattern. This vibration-free scanning is performed in a commercially available Michelson-Morley interferometer with dynamic alignment (BioRad FTIR). Scanning, alignment and data acquisition are all performed by this device. The operation of this interferometer is depicted schematically in Figure 4.2.

Unfortunately it is not possible to put a sample in one of the arms of the interferometer since the same optical path is traversed twice. Besides this, there is no room inside the BioRad to mount a sample and a set of lenses. For this reason two interferometers are used instead of one. The first interferometer is a Mach-Zehnder interferometer similar to the one shown in Figure 4.1 but with a fixed delay. The sample is located in one of the arms of this interferometer. The second interferometer is the BioRad which performs the scanning.

*The pulse entering the sample E_{s0} does not necessarily have the same shape as the reference pulse, even if the setup shown in Figure 4.1 is used, because the beam splitters can be (slightly) frequency dependent. Also the dispersion in both arms of the interferometer can be different, causing E_{s0} to differ from E_r.

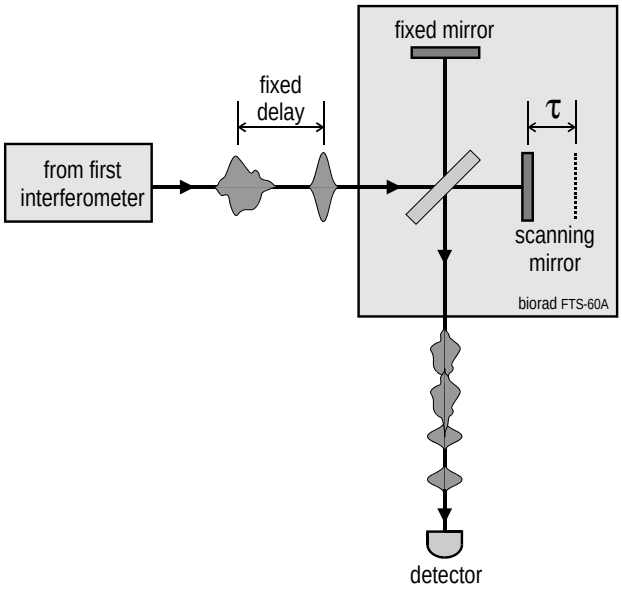

Figure 4.2: For practical reasons two interferometers are used instead of one. A beam containing the reference pulse and the signal pulse with a fixed time delay is constructed in the first interferometer. This interferometer is the same as was shown in Figure 4.1, only with a fixed delay. The second interferometer is responsible for scanning the delay.

If the time delay in the second interferometer equals the delay of the reference pulse in the first interferometer, the signal and reference pulses overlap and create a cross-correlate just as was explained in Section 4.2. When the time delay in the second interferometer is zero, both pulses interfere with themselves, yielding the sum of two autocorrelates, which is less interesting in this perspective.

The detailed realization of the first interferometer is shown in Figure 4.3. In addition to transmission measurements, this interferometer can also be used for reflection measurements if flipping mirror M4 is removed.

For an optimal signal to noise ratio, it is desirable to have a strong cross-correlate and a small offset I_0. This is the case when the amplitudes of signal and reference pulse are equal. If the detector is not saturated, however, a stronger reference signal can be used. This will act as an amplification of the signal, since the detector measures the product of the signal and reference pulse as described by Eq.(4.2), but it also increases the offset quadratically.

Since light leaving the sample is diffuse, only a small part is directed towards the detector (which is behind the BioRad). In this setup glass plates are used as beam splitters. These reflect approximately 4% of the light, causing the intensity in the reference path to be 625 times weaker than in the intensity in the reference path. This way it is compensated for that the amount of light leaving the sample in the direction of the detector is much smaller than the amount of incoming light.

The complete experimental setup, including the pulsed laser source, alignment laser and the two interferometers, is shown in Figure 4.4.

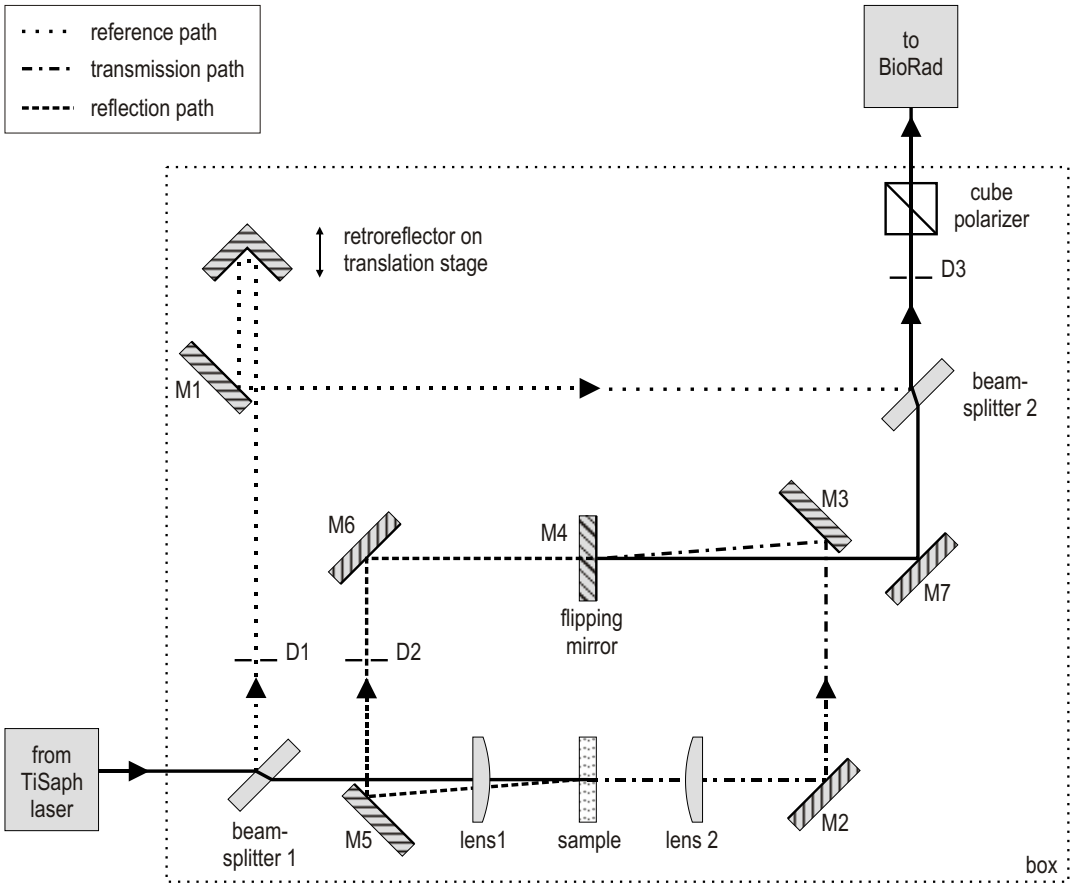

Figure 4.3: Detailed schematic of the Mach-Zehnder interferometer that was introduced in Figure 4.1. The reference path is formed by mirror M1 and the retroreflector. Mirrors M2, M3, M4 and M7 form the signal path for transmission measurements. In addition, this setup can be used for measuring the reflected light by removing M4. In this configuration M5, M6 and M7 form the signal path. By translating the retroreflector, both paths can be made approximately the same length so that the path length difference falls within the scanning range of the BioRad. The lenses are used to focus the light on the sample so that only a small area is probed and the speckle pattern is large. The diaphragms are used to select a single speckle spot (D2, D3) and to block undesired reflections from the back of the beam splitters (D1, D3). Finally, a polarizer selects vertical polarization because horizontally polarized light coming from the sample does not interfere with the reference and would only increase the bias.

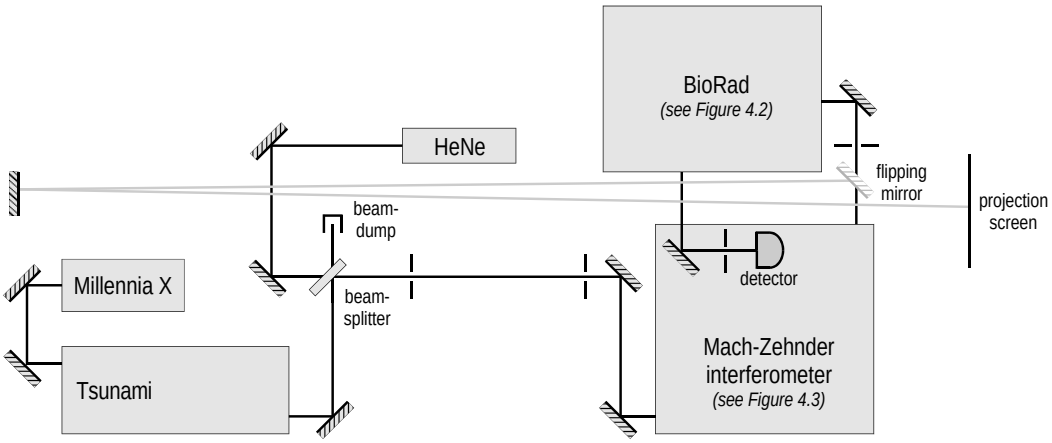

Figure 4.4: Complete setup used for the time-resolved measurements. A 10W crystal laser pumps a Titanium-Sapphire laser emitting 150 fs *pulses at a wavelength of* 775 nm *and a repetition rate of 82MHz. Of the total power of 2W, only 4% is used in the setup, the rest is blocked by a beam dump. A Helium-Neon laser provides a beam of visible light that is used for alignment. Two apertures at a large distance make sure that both laser beams overlap and always enter the setup in the same way. After the first interferometer, a flipping mirror was placed. If this mirror is flipped in, the beam leaving the interferometer is projected on a screen after propagating over four meters. The projection is used to align the signal and reference paths in the Mach-Zehnder interferometer. Finally, after passing through the second interferometer, the light reaches the detector which is in the same box as the first interferometer.*

4.4 Data processing

The BioRad has a computer interface that allows storing of the interferogram. Each file contains measurements on several positions of the sample, as well as a reference measurement made without sample in the signal arm. Before the time resolved intensity or the diffuse delay time can be calculated, the raw data needs several processing steps. These steps will be illustrated using data from a 10.1 μm thick sample. The reference measurement is shown in Figure 4.5 and the data for five different sample positions is shown in Figure 4.6. Typically 25 scans were made for the thinner samples up to 40 scans for the thicker samples. The BioRad scans with a resolution of approximately 4 cm^{-1}† corresponding to a scan range from -7.5 ps to 7.5 ps. The distance between two sample points is 80 nm, or 0.26 fs. This means that every scan has 56884 points of data.

4.4.1 Time domain filtering

The first step in processing the data is filtering in the time domain. This step isolates the desired cross correlate and removes the autocorrelate and undesired extra cross correlates. The cause of the extra cross-correlate was identified to be a thin coating on the detector. Pulses directly transmitted through this coating interfere with pulses that reflect internally twice before reaching the detector. Simply replacing all data outside the region of interest

†For the two thickest samples of 17.2 μm and 18.0 μm an asymmetrical scan with a resolution of 2 cm^{-1} was used, giving a time range from 0 ps to 15 ps

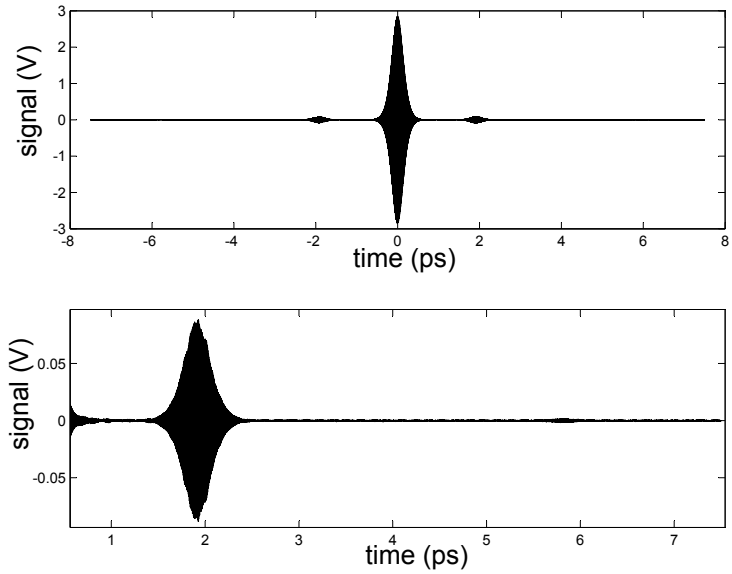

Figure 4.5: Interferogram belonging to a reference measurement without sample. The whole dataset is visible in the upper picture, showing an autocorrelate and two cross-correlates. The lower picture shows a zoom of the right cross-correlate. A small extra bump is present at 6 ps*, probably due to an undesired reflection from a thin coating. Furthermore, it can be observed that the cross-correlate looks somewhat dented, an effect that seems to be related to a slight misalignment of the setup.*

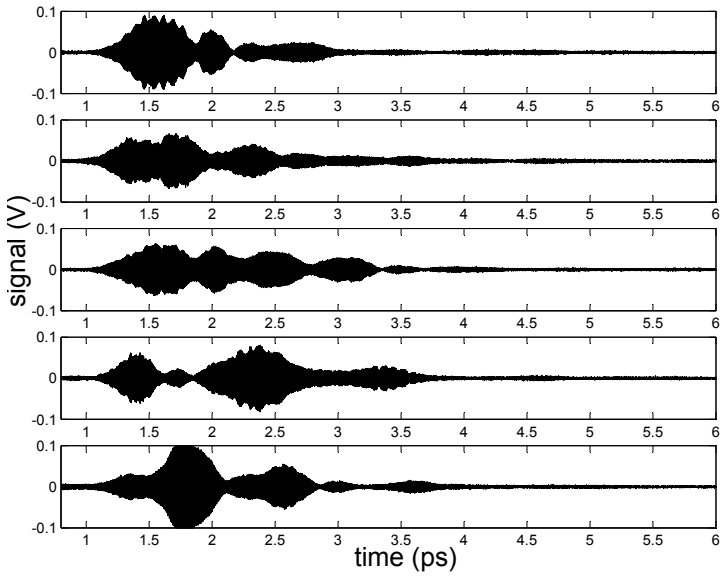

Figure 4.6: Interferograms belonging to a transmission measurement made at different positions of a 10.1 μm *thick* TiO_2 *sample. Between measurements the sample is translated further than this thickness of the sample (approximately* 30 μm*). Therefore the measurements can be interpreted as had they been performed on different realizations of a random material.*

by zero causes artefacts in the frequency domain. Therefore a smoother, trapezium shaped filter with a transition time of 0.5 ps is used.

The second step is to fix the time offset of the measurements. This is necessary since the samples that were used were on a substrate. The time delay in this substrate is not present in the reference measurement and therefore needs to be accounted for separately. Unfortunately it is not possible to make a reference measurement with an empty substrate since most samples completely cover the substrates. Also a reference measurement using a different, empty substrate will not work because this substrate cannot be placed at exactly the same angle as the real sample, causing a difference in substrate delay time.

To overcome these problems, the reflection part of the setup is used. Once the sample is in place, the light reflected from the front and back of substrate propagate through the reflection arm of the interferometer. At the BioRad they are cross-correlated, causing a peak in the interferogram at exactly the optical path difference d. Using the known refractive index of fused silica (n=1.454 at 775 nm [31]), the thickness of the substrate is found, $L_s = d/(2n)$. Therefore the extra delay time with respect to the situation without sample is $\Delta t = L_s(n-1)/c$, with c the speed of light in vacuum.

The accuracy of this process is determined by the error in the refractive index ($\pm$ 1e-3), together with the substrate flatness and reproducibility of the measurements (found a scatter in d of $\pm 0.5\ \mu$m). Together this yields an accuracy of ± 3 fs.

4.4.2 Calculating the transfer function

In Section 4.2 it was seen that to calculate the transfer function we have to deconvolve the measured signal with the reference measurement. Since a deconvolution is a division in the frequency domain, we have to transform the measured cross correlates to the frequency domain first. We use the full set of measurement data of 56884 points (everything except the cross correlate is zero because of the time filtering), perform a fast fourier transform[‡], and do the division.

Since in practice the source pulse only covers a limited frequency range, the signal is divided by almost zero outside the bandwidth of the source pulse, causing very strong noise outside this bandwidth. This effect can be seen in Figure 4.7. If we are interested in measurements in the frequency domain, such as the delay time $\phi'(\omega)$, only a portion of the measured transfer function can be used and the rest has to be discarded.

4.4.3 Frequency domain filtering

For measurements in the time domain such as measuring the intensity propagator $R(t)$, the transfer function has to be filtered before transforming it to the time domain; otherwise the noise outside the usable bandwidth would dominate the signal. The filter has to isolate the usable part of the transfer function and at the same time have a minimal impact on the shape of the signal in the time domain. Unfortunately there always is a tradeoff between sharp filtering in the frequency domain and a high resolution in the time domain.

We will use a filter of the Chebyshev family. These filters have the property that the side-lobes are constant and below a specified value, in this case -100dB. The filter function

[‡]For this the program Matlab 6.1 was used. The fast Fourier transform algorithm in this program can transform sets of data of an arbitrary length.

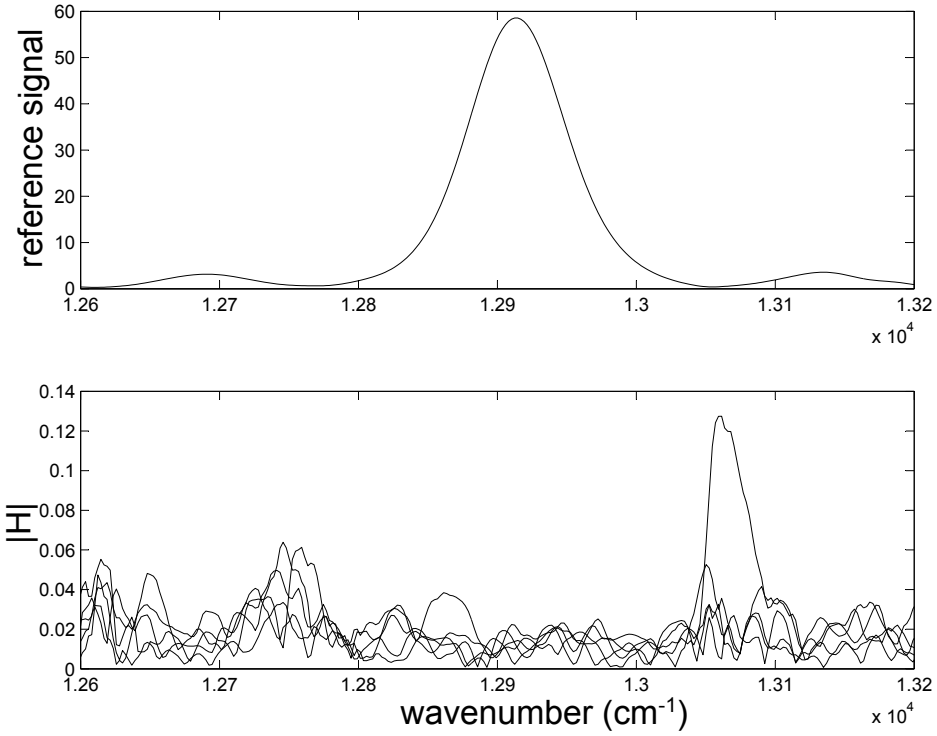

Figure 4.7: Amplitude of the reference measurement (top) and of the transfer function, H, at five different sample positions (bottom). Between approximately $12830\,\mathrm{cm}^{-1}$ *and* $13000\,\mathrm{cm}^{-1}$ *the reference measurement is large enough to calculate the transfer function. Outside this bandwidth, the reference signal goes to zero or has side-lobes caused by small misalignment. To calculate H, the sample signal is divided by the reference signal. Since outside the usable bandwidth both signals will have a very low amplitude, the noise will be dominant. This effect can be seen in the lower picture. The sidelobes in the upper picture are approximately* $222\,\mathrm{cm}^{-1}$ *away from the center. This will cause a modulation of the signal with a period of approximately* $150\,\mathrm{fs}$ *(the time it takes light to travel* $1/222cm$*) as was seen earlier in figures 4.5 and 4.6. Since the side-lobes will be filtered out this ripple has no effect on the final results.*

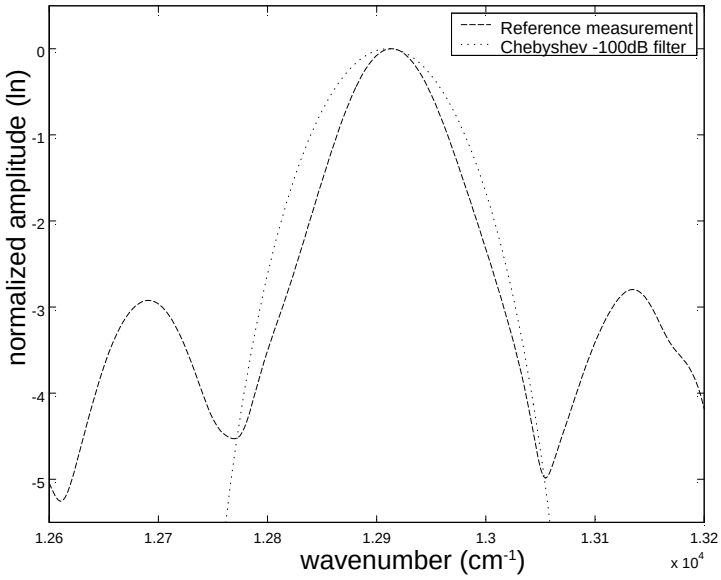

Figure 4.8: Amplitude spectrum of the reference measurement. The bandwidth of the Chebyshev filter (dotted line) is chosen in such a way that the sidelobes are filtered out and the central peak is preserved as much as possible.

and the reference measurement are shown in Figure 4.8 (frequency domain) and Figure 4.9 (time domain).

4.4.4 Fitting the intensity

After filtering with the Chebyshev filter, the transfer function can be transformed to the time domain. Only the positive frequencies are taken into account here. Finally the time resolved intensity is obtained by squaring the amplitude of this function. Averaging the intensity over many sample positions yields the average intensity transfer. For a 10.1 μm thick sample this function is plotted in Figure 4.9.

The diffuse traversal time can be extracted from this data by calculating $\int dtI(t)t$. This method gives $\tau_d = 0.73\,\mathrm{ps}$. According to equation (3.23), for large t, the transmitted intensity should decay as $\exp(-\pi^2 D/L'^2)$. Fitting the graph from $t = 0.5\,\mathrm{ps}$ to $t = 6.2\,\mathrm{ps}$ the value $L'^2/(6D) = 0.85\mathrm{ps}$ is found. The diffuse traversal time can be found by correcting for surface effects (see Eq. (A.30)). For these samples, the correction equals 0.12 ps and therefore we find $\tau_d = 0.73\,\mathrm{ps}$.

4.4.5 Analyzing the field statistics

Examination of the intensity transmission gives much information about the diffusion process. This measurement method, however, enables us to analyze the phase information as well. In Section 3.5 the statistical properties of the phase were derived. The base of this derivation is that the measured complex transmission coefficient, $H(\omega)$, obeys Gaussian statistics.

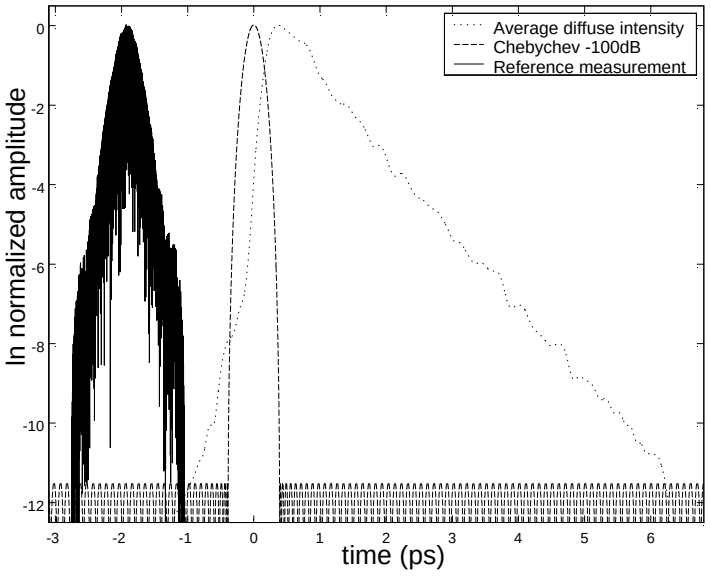

Figure 4.9: Comparison of the time dependent intensity of the incoming pulse (reference measurement), the transmitted intensity and the Chebychev filter. After deconvolution and filtering, the Chebyshev filter will act as the new input pulse. It can be seen that the sidelobes of the filter are constant and small enough not to distort the signal. The full width at half maximum of the reference pulse is 310 fs. *For the filter this width is* 250 fs.

For a Gaussian distribution, three conditions have to be met; the phase has to have a uniform distribution and the intensity has to have a Rayleigh distribution (Eq. (3.30)). Furthermore, the phase and intensity have to be uncorrelated variables.

In the analysis of the measurements, we assume the statistics to be equal for the whole bandwidth of the measurement. Data is collected in the frequency range between 12821 cm^{-1} and 13300 cm^{-1}. This leads to 80 points of data per sample position.

The probability distributions of ϕ and I are plotted in Figure 4.10 and Figure 4.11. The correlation coefficient of the real and the imaginary part of the transfer function $C_{RI} \equiv \langle \mathrm{Re}\{H\}\,\mathrm{Im}\{H\}\rangle / (\langle \mathrm{Re}\{H\}\rangle \langle \mathrm{Im}\{H\}\rangle)$ was found to be smaller than 0.05%, suggesting that the amplitude and phase are not correlated. From this we find it justified to apply the theory from Section 3.5, which it assumes Gaussian statistics.

4.4.6 Calculating the delay time statistics

In Section 3.5.2 the probability distribution of the diffuse delay time, ϕ', was predicted. To find the diffuse delay time first the phase of the transfer function is calculated. The derivative, ϕ', could now be found by calculating $[\phi(\omega_{n+1}) - \phi(\omega_n)]/\Delta\omega$. This method, however, poses a problem since the phase is 'wrapped around' on the interval $\langle -\pi, \pi]$. A phase difference Δ between $\phi_1 = \pi$ and $\phi_2 = \pi + \Delta$ would be interpreted as a difference of $\Delta - 2\pi$.

To correct this problem, phase differences between consecutive data points are raised or lowered by 2π to get the lowest absolute value of the phase derivative,

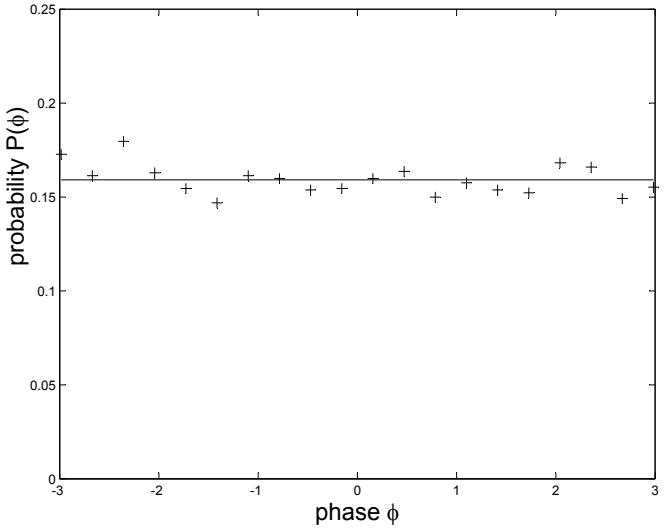

Figure 4.10: Probability density of the phase. The phase of the transmitted light is distributed uniformly over $\langle -\pi..\pi]$. If a coherent beam were present, this would cause a deviation from this distribution. The uniform distribution is a necessary condition for the zero mean Gaussian model that was used in Section 3.5.

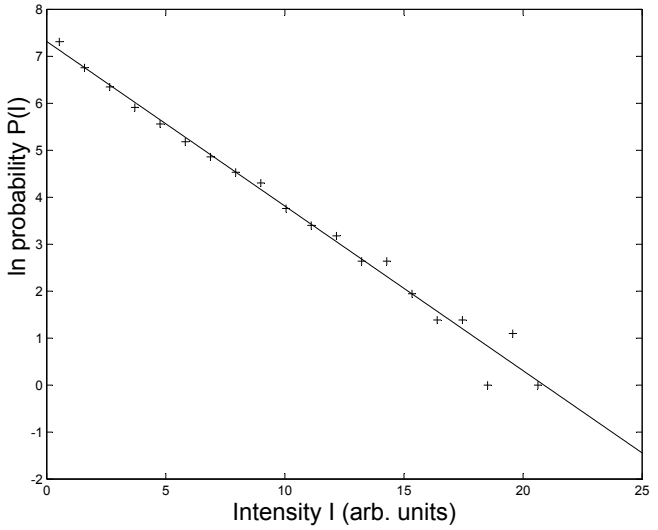

Figure 4.11: Probability distribution of the transmitted intensity. The distribution matches the Rayleigh distribution (solid line) that was found from the assumption of Gaussian statistics of the field (see Eq. (3.30)*).*

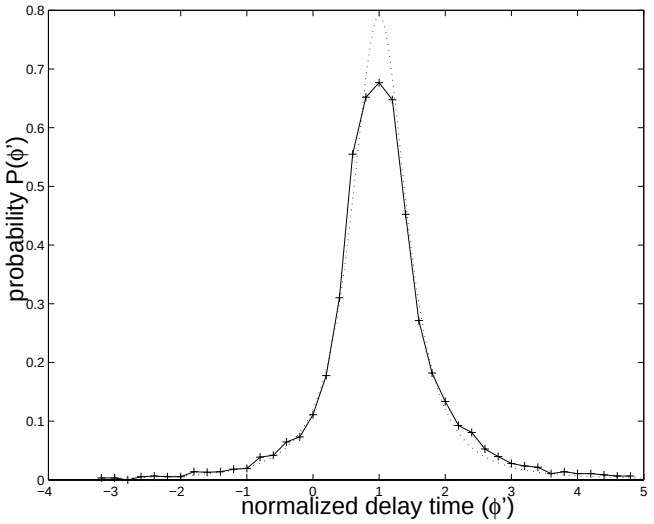

Figure 4.12: Probability distribution of the delay time ϕ' for a $10.1\,\mu$m *thick sample, measurements are connected by a solid line to guide the eye. The dotted line is the theoretical curve for* $Q = 0.4$. *The measured distribution clearly corresponds to a higher value of Q (which causes a wider distribution). This agrees with the prediction in Eq.* (A.34) *and is an indication that edge effects play a role in the transmission through this sample.*

$$\phi'_{\text{jumps}}(\omega_n) = \frac{\phi(\omega_{n+1}) - \phi(\omega_n)}{\Delta\omega} \tag{4.7}$$

$$\phi'(\omega_n) = \phi'_{\text{jumps}}(\omega_n) - 2\pi\text{round}\left(\frac{\phi'_{\text{jumps}}(\omega_n)}{2\pi}\right) \tag{4.8}$$

This procedure limits the possible values of ϕ' to $\langle -\pi/\Delta\omega, \pi/\Delta\omega]$. In the unlikely case that the phase derivative lies outside this interval, the wrong value is measured. The probability for this to happen can be calculated from Eq. 3.44 and the scanning range of the BioRad. For the $10.1\,\mu$m sample this happens in only 0.55% of the cases and therefore this limitation will not be corrected.

A further limitation of this method is found in asymmetrical scans. In these scans only positive time values are recorded. The largest delay time that can be found corresponds to the width of the time window ($t_{\max}$). Unfortunately with this method of calculating the phase derivative, delay times larger than half this value will be interpreted as negative times. This problem is avoided by doubling the width of the time window by appending zeros for $t < 0$.

The measured $\phi'(\omega)$ can be used to calculate $W = |H(\omega)|^2\phi'(\omega)$. From the average values of ϕ' and W, delay times of respectively 0.71 ps and 0.72 ps are found. The normalized probability density functions are shown in Figure 4.12 and Figure 4.13.

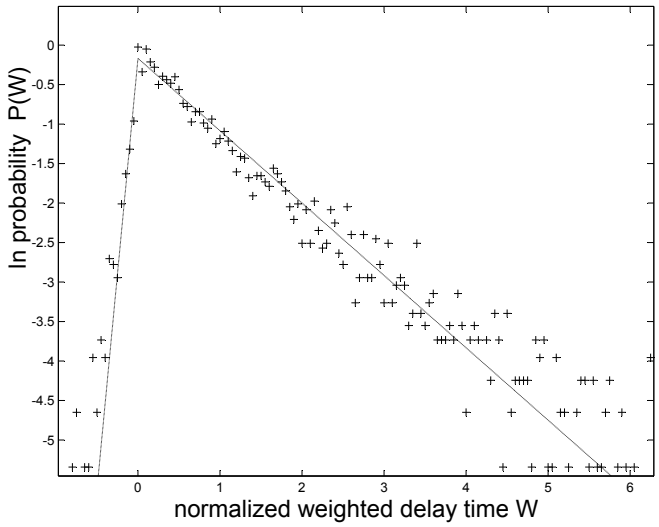

Figure 4.13: Probability distribution of the delay time W for a 10.1 μm *thick sample. The solid line is the theoretical curve for $Q = 0.4$. The top of the distribution is at $W = 0$, indicating there is no time offset. Again the $Q = 0.4$ does not fit, but a higher value gives a better fit. It appears that the curve is not completely straight for $W > 0$. This effect will be investigated in the following chapter.*

4.4.7 Analyzing the delay time statistics

Finally the parameter a and Q can be extracted from the data. Table 4.2 shows several important statistical properties of the functions $P(\phi')$ and $P(W)$. They are derived from equations (3.44) and (3.48) by performing the appropriate integrations.

The parameter a equals the diffuse delay time τ_d and is obtained from the distributions easily since it is the average of ϕ' and of W. Because $P(\phi')$ is symmetrical around $\phi' = \langle\phi'\rangle$, the median of ϕ' should also give a. The difference between the median and the mean of ϕ' is a measure of the asymmetry of the distribution. We can calculate an asymmetry factor $s \equiv (\langle\phi'\rangle - \phi'_{\mathrm{med}})/\langle\phi'\rangle$, where ϕ'_{med} is the median of ϕ, meaning that the number of values measured above this number equals the number of values below. For this sample we find an asymmetry smaller than 0.5%, indicating no deviation from Gaussian statistics. Mechanisms that break the symmetry of this distribution will be discussed in Chapter 5.

Parameter Q can be extracted from the distributions of ϕ' and W in many ways. In principle every equality in Table 4.2 containing Q can be used. If the measurements obey Gaussian statistics (as was assumed in Section 3.5) all methods give the same value for Q. A time offset, t_0, in the measurements could, however, affect the probability distributions. This will cause $P(\phi')$ and $P(W)$ to shift over t_0. In the probability distribution of ϕ' this has the same effect as renormalizing the parameters $a \rightarrow a' = a + t_0$ and $Q \rightarrow Q' = Qa^2/(a + t_0)^2$ (see Eq.(3.44)).

As opposed to $P(\phi')$, the weighted delay time distribution $P(W)$ is affected in a unique way. The time offset can be found by looking at the top of $P(W)$. Without time offset, this top is at $W = 0$. Since an offset shifts the distribution, the top is shifted to $W = t_0$.

Using different equations from Table 4.2, different values of Q are found. The results

method	$P(\phi' > 0)$	$\langle \phi' > 0 \rangle$	$\langle \phi' > \langle \phi' \rangle \rangle$	$\langle W > 0 \rangle$	$\langle W > \langle W \rangle \rangle$	var(W)
equation	4.10	4.12	4.13	4.17	4.18	4.19
Q	0.448	0.480	0.487	0.460	1.122	0.839

Table 4.1: Six different methods to extract Q from the delay time distributions. The last two methods give significantly different values for Q. These values depend on high values of W only and are more sensitive to measurement errors, statistical spread and possible non-Gaussian statistics.

are summarized in Table 4.1. As can be seen, all methods except the last two give results around $Q = 0.47$. The last two methods are highly influenced by large values of W. Since there are relatively few of those values spread over a large range, a large statistical error can be expected. The value of $P(W > \langle W \rangle)$ that was extracted from the measurement was lower than expected. For this value, Eq. (4.16) did not have a solution.

Large values of W are mainly caused by a high intensity. This can be seen by comparing ϕ' and $|H|^2$ for measurements corresponding to high values of W ($W > \langle W \rangle$) to their average value. We find ϕ' to be 20% higher than average, whereas the intensity for high values of W is 100% higher than average. Since an error in determining the amplitude affects high intensities more than low intensities, this is an extra reason not to rely on large values of W for fitting the curve.

4.5 Specifications

Apart from the noise and uncertainties introduced by the measurements, there also is a scatter in all measured parameters since the sample is a random material. The magnitude of this scatter is far larger than the other errors (except for very thin samples where the blurring effect of the Chebychev filter is more important). The effect of this scatter scales inversely with the square root of the number of measurements. The errorbars on the data (as presented in Chapter 5) are obtained by calculating the standard deviation of the spread and dividing by the root of the number of measurements.

4.6 Summary

An interferometric setup was used to measure intensity and phase of light that propagated through a slab of disordered material. The setup uses two separate interferometers, the first creates a beam containing a reference pulse and a pulse that propagated through the sample. The second interferometer performs stabilized scanning creating a cross-correlate of the signal and reference pulses. With the proper data-processing techniques, it is possible to extract the transfer function of the disordered sample from these measurements.

Using the data from a 10.1 μm thick slab as an example, the data processing required to find the time resolved intensity and the delay time statistics was explained. Special attention is required to compensate for the effect of the substrate and to optimize frequency domain filtering.

The measurements showed that the phase and intensity distributions of the transmitted light agree with Gaussian statistics. The theoretical predictions made in Section 3.5

average ϕ' (=median ϕ)	$\langle\phi'\rangle$	$= a$	(4.9)
probability ϕ' positive	$P(\phi' > 0)$	$= \frac{1}{2} + \frac{1}{2\sqrt{1+Q}}$	(4.10)
probability ϕ' above average	$P(\phi' > \langle\phi'\rangle)$	$= \frac{1}{2}$	(4.11)
mean of ϕ' above 0	$\langle\phi' > 0\rangle$	$= a\sqrt{1+Q}$	(4.12)
mean of ϕ' above average	$\langle\phi' > \langle\phi'\rangle\rangle$	$= a(1+\sqrt{Q})$	(4.13)
average W ($\neq$ median W)	$\langle W\rangle$	$= a$	(4.14)
probability W positive	$P(W > 0)$	$= P(\phi' > 0)$	(4.15)
probability W above average	$P(W > \langle W\rangle)$	$= \left[\frac{1}{2} + \frac{1}{2\sqrt{1+Q}}\right] \exp\left(\frac{-2}{1+\sqrt{1+Q}}\right)$	(4.16)
mean of W above 0	$\langle W > 0\rangle$	$= \frac{1}{2}a\left(1+\sqrt{1+Q}\right)$	(4.17)
mean of W above average	$\langle W > \langle W\rangle\rangle$	$= \frac{1}{2}a\left(3+\sqrt{1+Q}\right)$	(4.18)
variance of W	$\mathrm{var}(W)$	$= a^2\left(1+\frac{Q}{2}\right)$	(4.19)

Table 4.2: Statistical properties of the $P(\phi')$ and $P(W)$ distributions. A time offset can be incorporated in $P(\phi')$ (all formulas in the upper half of the table) by replacing $a \to a' = a + t_0$ and $Q \to Q' = Qa^2/(a+t_0)^2$. Equations 4.16 and 4.19 do not depend on a possible time offset, but are very sensitive to measurement noise and statistical noise.

Dynamic range	60dB
Center wavelength	12912 $\mathrm{cm}^{-1} \to$ 774 nm
Bandwidth	220 $\mathrm{cm}^{-1} \to$ 13 nm
Width of time window	12 ps
Time offset accuracy	3 fs
Time resolution	0.1 ps
Accuracy $\frac{L'^2}{6D}$ from slope fit $\log(I)$	0.1 ps $\pm$ 5% of the measured value
Accuracy τ_d from $\int dtI(t)t$	0.1 ps
Accuracy τ_d from $\langle\phi'\rangle$	3 fs

Table 4.3: Specifications of the time-resolved field measurements. The time resolution of 0.1 ps *is the full width at half maximum of the squared amplitude of the Chebychev filter. Details smaller than this value will be smeared out, also limiting the accuracy of τ_d obtained by integrating the intensity. The error of the slope fit is estimated by making a linear fit of the first and the last half of the slope. All accuracies are given without the statistical error.*

closely match the measured delay time distributions. Both the diffuse delay time and the dimensionless parameter Q were seen to be affected by edge effects as was predicted.

Chapter 5

Experimental results

Using the measurement setup that was described in the previous chapter, it is possible to test the theory presented in Chapter 3. In this chapter we will analyze the data, looking at both intensity and phase characteristics.

A recurring parameter in this analysis is the diffuse travel time (see Eq.3.25). This parameter can be found either directly from the measured intensity or indirectly from the slope of the intensity or from the phase statistics. Since the different analysis techniques are performed on the same set of data, this is a clean way of testing different aspects of diffusion theory. In particular the times found by fitting the intensity slope will be compared to the results from the three other methods (integrated intensity, average phase delay, and average weighted phase delay, see sections 3.4.2 and 3.5). The first time is proportional to $(L')^2$, whereas the other times have an offset that does not depend on the thickness of the sample, as was found in Eq.(A.30).

The phase measurements will provide diffuse delay times that can be compared to the values obtained from intensity measurements. Furthermore, the phase statistics are shown to provide information about the time offset and variations in sample thickness. This extra information is indispensable when analyzing small differences in the diffuse delay time.

In addition to the delay time, the dimensionless Q parameter was shown to be sensitive to surface effects. Different methods of extracting Q from the measurements are compared and will be used to test the newly developed theory (Eq.(A.34)).

Finally the measurements on the thinnest samples are expected to show a contribution of the coherent beam. The effect of this contribution will be analyzed and is compared to theoretical predictions.

5.1 Samples

The samples that are used were made by Rik Kop in 1997 [32, 14]. They consist of TiO_2 particles, with a refractive index of approximately 2.7, on the basis of commercially available rutile pigment. The diameter of the particles is 220 ± 70 nm. Samples with different thicknesses were made by smearing a suspension of particles on a 3mm thick fused silica substrate. The thickness was determined using an optical microscope with an accuracy of $\pm 0.3\ \mu$m. In the experiments samples with a thickness between 1.5 μm and 18.0 μm were used.

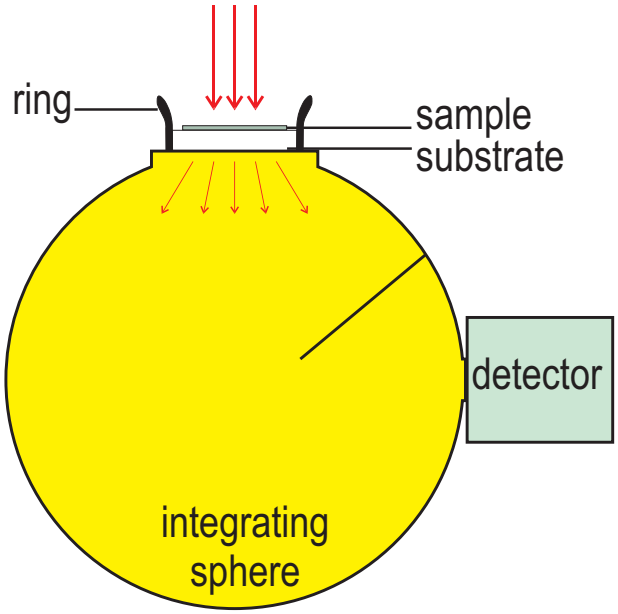

Figure 5.1: Setup used for total transmission measurements. Light is incident on a sample that is on top of an integrating sphere. The samples are on a substrate, mounted in a ring. The integrating sphere collects all light that is transmitted through the sample. This light is scattered multiple times before reaching the detector so that the detector signal does not depend on the original direction of the light and all directions contribute evenly. This way the light leaving the samples is integrated over all angles. The black line inside the integrating sphere represents the baffle, a partition to prevent light to hit the detector without being scattered. In this configuration, however, it does not prevent the light from hitting the detector after a single scattering event, which leads to incorrect reference measurements.

The mean free path of the samples was determined by measuring the total transmission as a function of sample thickness; according to Eq.(3.24) the transmission scales with $(z_{e1}+\ell)/L$. In this stationary measurement, both internal reflections at the sample surfaces and internal reflections at the substrate surfaces have to be taken into account. These reflections are incorporated in an effective reflectivity [33],

$$R_{\text{eff}} = \frac{R_{ab} + R_{bc} - 2R_{ab}R_{bc}}{1 - R_{ab}R_{bc}}, \tag{5.1}$$

where R_{ab} is the reflection coefficient at the boundary of the sample and the substrate and R_{bc} is the reflection coefficient for the substrate-air interface. The effective reflectivity is used to calculate the extrapolation lengths for the stationary measurements. Using Mie theory to estimate an effective refractive index of $n_{\text{eff}} = 1.34$ [32] and Fresnel's Law to calculate the reflectivities, we find an extrapolation length of $z_{e1} = 1.71\ell$ for the substrate-sample boundary and a length of $z_{e2} = 1.77\ell$ for the sample-air boundary.

The total transmission was measured using the setup in Figure 5.1. A bare substrate was used as a reference for 100% transmission* and the reflection from the integrating

*Actually, this is not the correct procedure since the reflection from the substrate is already incorporated

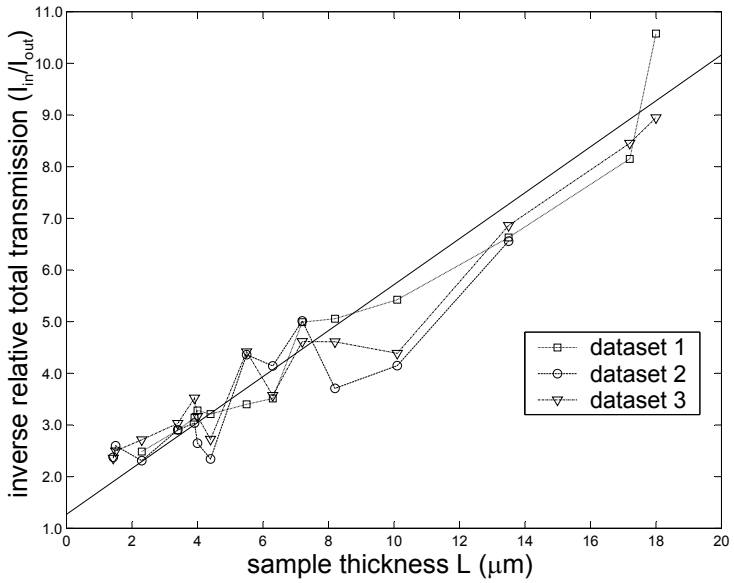

Figure 5.2: Results of the total transmission measurements. The measurements in dataset 1 were performed after creating the samples, the other measurements were performed later. Dataset 3 is the most recent. The datapoints are connected by lines to guide the eye. The inverse transmission is plotted, because this value is predicted to be proportional to $L/(z_{e1}+\ell)$. The solid line is a linear fit to the first dataset, yielding $\ell = 0.97\ \mu$m.

sphere back to the sample is neglected. The results of these measurements are plotted in Figure 5.2 (dataset 3) including earlier measurements on the same samples dataset 1 [14] and dataset 2 [34]. Unfortunately after performing the measurements it was discovered that with a bare substrate, the light coming out of the integrating sphere is not completely diffuse. A contribution arising from single scattering of the laser beam is also present and causes the reference value to be too high. The difference with the other measurement is approximately a factor of 1.25 (found by overlapping the linear fit of the curve at L=0). After correcting with this factor the three sets of data overlap reasonably well. The second series of measurements differ from the first measurements performed on the samples (dataset 1). The latest data shows this deviation is reproducible to a large extent, suggesting that the samples have deteriorated since they were created[†].

Dataset 2 is used to find the mean free path. A fit of the slope of the inverse of the transmission gives $\ell + z_{e1} = 2.63\ \mu$m and therefore $\ell = 0.97\ \mu$m[‡]. The zero crossing is at 1.27 corresponding to $(\ell + z_{e1})/(z_{e1} + z_{e2}) = 0.79$, which is in good agreement to the value of 0.78 obtained using the calculated extrapolation lengths. For this fit, the measurement

in the extrapolation length by means of Eq.(5.1)

[†]In fact some time resolved measurements showed a pulse that was transmitted through the sample without delay or deformation, suggesting a hole in the sample. These measurements were removed from the time resolved data, but in the total transmission measurement a larger area was illuminated so that such a correction is impossible.

[‡]Coincidentally, this is almost equal to the value of $\ell = 0.95\ \mu$m found in [14]. In this paper a different values was used for the extrapolation length because substrate reflections were not taken into account.

on the 18.0 μm sample was disregarded[§]. With a wavelength of 775 nm this gives $k\ell \approx 8$ meaning the samples are not localizing light.

In the dynamic measurements internal reflections of the substrate are irrelevant since they occur with a large time delay (corresponding to twice the 3mm thickness of the substrate). Therefore the substrate is considered to be semi-infinite for calculating these boundary conditions and we find the dynamic extrapolation length $z_{e1} = 0.69\ell$.

5.2 Diffuse delay time

In Chapter 4 four methods were treated to extract the diffuse delay time τ_d from the measurements. The results of applying these methods to samples with a different thickness is shown in Figure 5.3[¶]. These data show that the value for $(L')^2/(6D)$ found from fitting the slope of the intensity is significantly higher than the diffuse delay time found using the three other techniques.

The difference is about 0.12 ps for the first 6 samples. This value is in good agreement with the edge effects predicted in Eq. (A.30) using an ejection depth of $z_{\text{ej}} = \frac{2}{3}\ell$ as suggested in [9]. For $z_{\text{ej}} = \ell$ we find a time of 0.14 ps and for $z_{\text{ej}} = 0$ this value would be 0.07 ps. This suggests that $\frac{2}{3}\ell$ is the correct value for the ejection depth. The accuracy, however, is not high enough to rule out values of $z_{\text{ej}} = \ell$ or $z_{\text{ej}} = 0$. In Figure 5.4, the diffuse traversal time obtained from fitting the slope of the intensity is corrected for an edge effect of 0.12 ps.

To be certain that this effect causes the time difference, other influences have to be ruled out. One of this influences could be an offset on the time axis. If somehow $t = 0$ in the measurements is not correct, for example if there is an error in the correction for the substrate thickness, all techniques except the slope fit will produce erroneous values. In the following section it will be shown that this possibility can be ruled out by carefully examining the phase statistics.

Comparing the three other measurements that results obtained from the measured phase are consistent with the results from the measured intensity. This is a strong indication that the speckle theory developed in [18] is valid. Furthermore it shows that the data processing is performed correctly and that no errors are introduced by the filtering process or the calculation of the phase derivative.

Figure 5.5 shows the square root of the diffuse traversal time raised by the edge effect correction time of 0.12 ps for $z_{\text{ej}} = 2\ell/3$. This correction time has to be added to the diffuse delay time in order to find $(L')^2/(6D)$ (see Eq. 3.25). From this graph the total extrapolation length, $z_{e1} + z_{e2}$, and the diffusion constant, D, can be obtained. The results, together with the results obtained using a correction time of 0.07 ps for $z_{\text{ej}} = 0$, are summarized in Table 5.1. If the correction time is calculated using $z_{\text{ej}} = 0$, the value for the total extrapolation length obtained from the fit is consistent with the calculated

[§]For thick samples, the spot of diffuse light leaving the sample can be larger than the opening of the integrating sphere, causing a lower transmission to be measured.

[¶]All measurements were performed as described in the previous chapter, except for the measurement on the 1.5 μm thick sample where it was possible to perform the reference measurement on a empty part of the substrate and the measurement on the 4.0 μm thick sample where an bare reference substrate was used.

		$\langle W \rangle$	$\langle \phi' \rangle$	$\int dt I(t) t$	slope $\ln I(t)$
$z_{\mathrm{ej}} = 2\ell/3$	$z_{e1} + z_{e2}(\ \mu\mathrm{m})$	3.4	3.8	3.3	2.3
	$D(\ \mathrm{m^2 s^{-1}})$	31.7	33.6	30.3	24.6
$z_{\mathrm{ej}} = 0$	$z_{e1} + z_{e2}(\ \mu\mathrm{m})$	2.5	2.7	2.5	2.3
	$D(\ \mathrm{m^2 s^{-1}})$	29.2	31.0	28.0	24.6

Table 5.1: Total extrapolation length and diffusion constant as obtained from fitting the square root of $\tau_d + \tau_e$. Using $z_{ej} = 2\ell/3$, the values for the diffusion constant are in good agreement with the value of $32 \pm 2\,\mathrm{m^2 s^{-1}}$ as found in [14], except for the value obtained from fitting the intensity slope. All values are very far away from the $11.7 \pm 1\,\mathrm{m^2 s^{-1}}$ found from the intensity correlation function of samples similar to the ones we use [35]. If $z_{ej} = 0$ is used, however, the total extrapolation lengths are close to the calculated values and the diffusion constants are closer to the value obtained from the intensity slope.

values.

Since fitting the slope of the intensity directly gives us $(L')^2/(6D)$, it is not necessary to correct this value and the diffusion constant and extrapolation lengths can be found directly. The extrapolation length of 2.3μm that is found this way is close to the calculated value of $(0.79 + 1.77)0.97\ \mu\mathrm{m} = 2.5\ \mu\mathrm{m}$.

5.3 Field statistics

The delay time statistics are based on the assumption that the field has a Gaussian distribution. Before analyzing the delay time, we will first test if this assumption is valid. In analyzing the distributions of the phase and the intensity, deviations from Gaussian statistics were found for the thinnest samples. The phase distribution is not uniform, as can be seen in Figure 5.6, and the intensity has no Rayleigh distribution (Figure 5.7). To analyze the deviations from Gaussian statistics, we will examine $\langle H(\omega) \rangle$. This function should correspond to coherent propagation, but only if enough measurements are made to average out the incoherent contribution.

A polar plot of every measurement of $H(\omega)$ performed on the 1.5 μm thick sample is shown in Figure 5.8. It is clearly visible that the curves are not centered around the origin as expected when there is no coherent contribution. Therefore we conclude there is a coherent contribution present. The function $\langle H(\omega) \rangle$, which is plotted in Figure 5.9 should in principle contain the group velocity and the phase velocity of the coherent beam. Unfortunately the contribution of the incoherent propagation is still quite large (if not, the plot would be a single curve without loops). Therefore it is not possible to interpret the phase derivative of this function as L/v_{gr}. It is possible, however, to extract the phase velocity.

The 1.5μm sample was different from the other samples because not all of the substrate was covered by the sample. Therefore it was possible to perform the reference measurement with the substrate in place, instead of having to deduce the thickness from a reflection measurement. This means that the error in the time offset is much smaller than 3 fs. At a wavelength of 775 nm, an uncertainty of 3 fs corresponds to a phase delay of approximately 2π, so for this sample the error will be much smaller than that. Therefore we can interpret

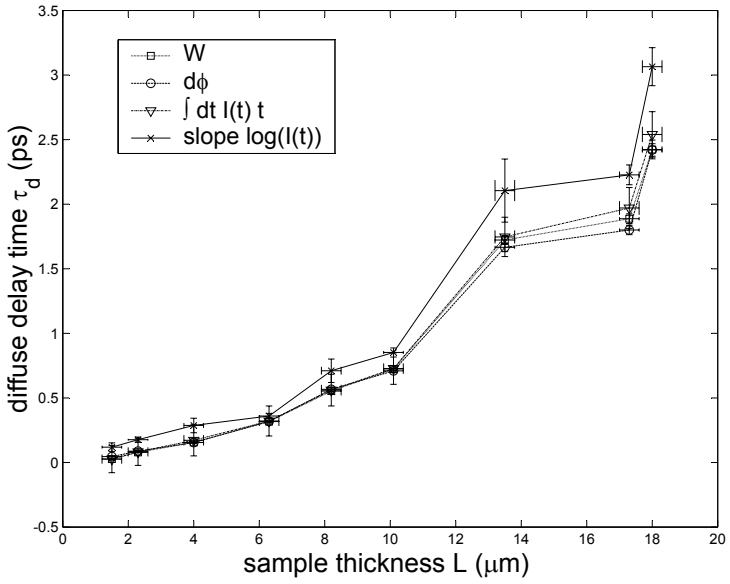

Figure 5.3: Comparison of four methods of extracting the diffuse traversal time τ_d from the measurements. The values obtained from the slope fit equal $\tau_d + \tau_e$ and are seen to be significantly higher than the values obtained by other methods.

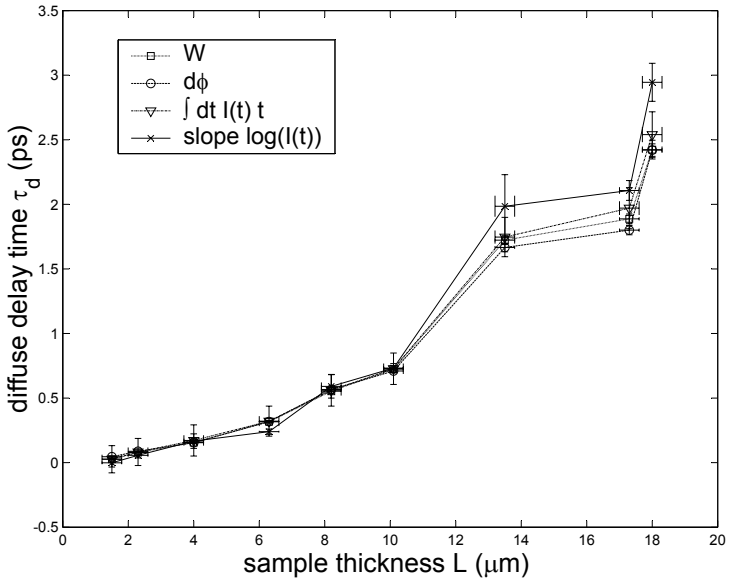

Figure 5.4: Four methods of calculating the diffuse traversal time τ_d. In this plot the values obtained by fitting the slope of $\ln I(t)$ are compensated for the edge effects by $\tau_e = 0.12\,\mathrm{ps}$. For samples up to $10.1\,\mu\mathrm{m}$ this is in excellent accordance with the values obtained by other methods.

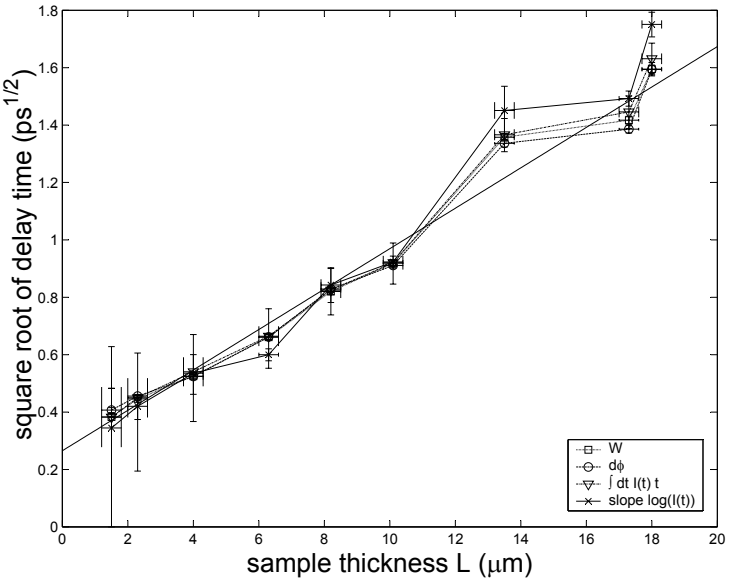

Figure 5.5: Square root of the diffuse traversal time τ_d raised by the correction for edge effects of 0.12 ps. *The straight line is a fit to $\sqrt{\langle\phi'\rangle}$; these values have the smallest errorbars. The slope of the fit equals $1/\sqrt{6D}$, yielding $D = 33.6\,\mathrm{m^2 s^{-1}}$, which is in good agreement with the value 32 ± 2 found in [14]. The intersection with the x-axis gives $z_{e1} + z_{e2} = 3.8\,\mu$m, which differs from the calculated value of $2.5\,\mu$m.*

the average phase of the transfer function as being the phase delay L/v_ϕ plus or minus an integer number of 2π. We find a phase velocity of $v_\phi = c/n_{\mathrm{eff}} = c/(1.34 \pm 0.5m)$, where m is a unknown integer number that could be zero. It is hard to estimate the uncertainty for this single measurement, so it cannot be said if the excellent agreement to the theoretical estimation of $n_{\mathrm{eff}} = 1.34$ is coincidental.

Finally $\langle H(\omega)\rangle$ is plotted for an $8.2\,\mu$m thick sample (Figure 5.10). Here it appears that there are two contributions, one is a field with a short time delay of 0.16 ps (slow rotation), while the other contribution has a longer time delay of 1.07 ps (fast rotation). These rotations are equivalent to two peaks in the time domain average transfer function. The times neither corresponds to the expected coherent traversal time ($= L/(n_{\mathrm{eff}}c) = 20$fs) nor to the average traversal time ($\tau_d = 0.56\,$ps). It is not clear what is causing these peaks.

5.4 Delay time statistics

The probability distributions of ϕ' and W contain a lot of information. In this section the experimentally obtained distributions will be examined in detail. The theoretical distributions are given by Eq. (3.44) and (3.48). They depend on two parameters, Q and a, where $a = \langle\phi'\rangle = \langle W\rangle = \tau_d$ and $Q \approx 0.4$. Absorption causes Q to decrease and, as we show in Appendix 3.4.2, edge effects cause an increase in Q. The values of a and Q corrected for edge effects are given by equations (A.30) and (A.34). To test this new theory we will investigate the delay time statistics and extract these parameters.

Figures 5.11, 5.12 and 5.13 show the normalized distributions extracted from the mea-

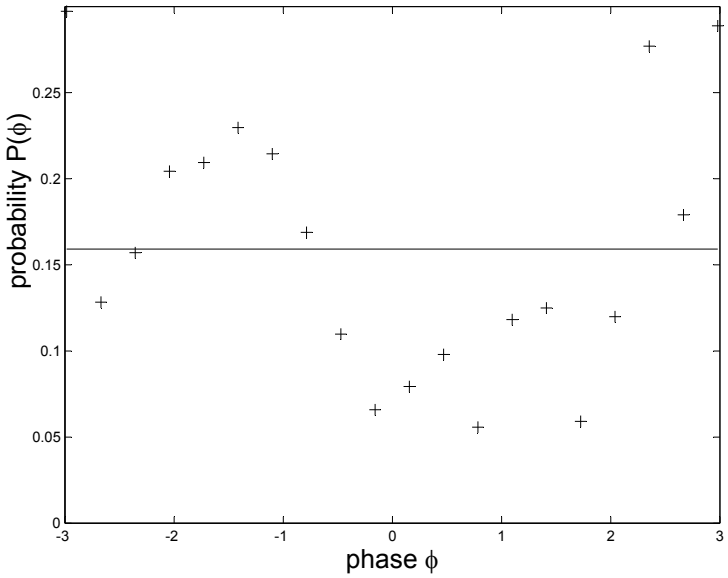

Figure 5.6: The phase of the transfer function for the thinnest sample ($1.5\,\mu\mathrm{m}$*) is not distributed uniformly. From this it can be concluded that the assumption of Gaussian statistics is not valid for this sample.*

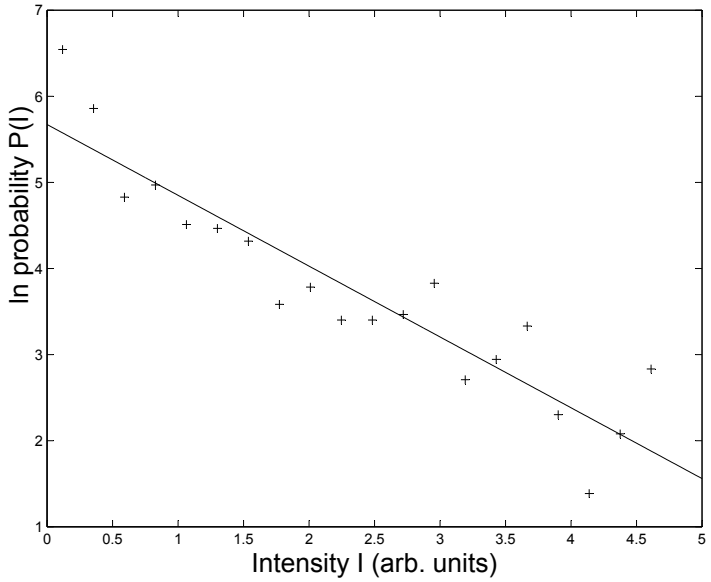

Figure 5.7: Probability density of the transmitted intensity for a $1.5\,\mu\mathrm{m}$ *thick sample. The solid line is a linear fit to logarithm of the probability density. If the transmitted light would obey Gaussian statistics, a Rayleigh distribution (Eq.* (3.30)*) is expected and the points would lie on this line (see Figure 4.11). For this sample, however we find a different probability function with a higher probability for lower intensities. The deviation can be seen in the first two datapoints; since these two points together represent over 50% of the measured intensities and since they are a factor 1.5 to 2.5 higher than expected, this is a significant deviation.*

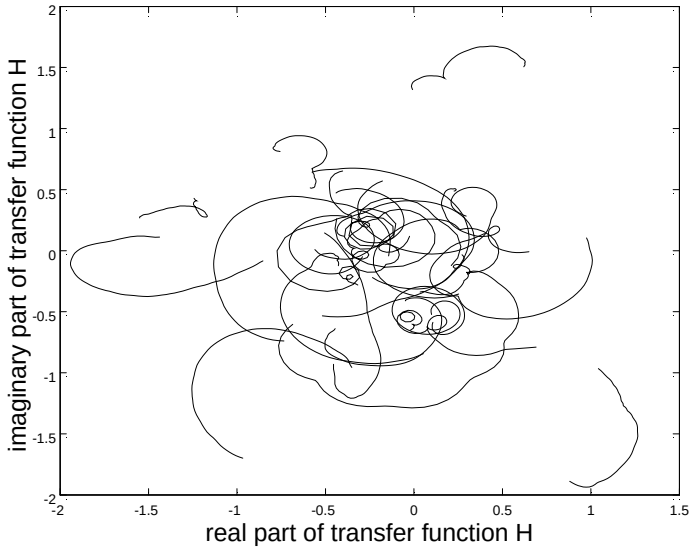

Figure 5.8: Polar plot of 23 different measurements of the transfer function of the $1.5\ \mu\mathrm{m}$ *thick sample. In this plot the phase of the field is represented by the angle with the x-axis and the amplitude is the distance to the origin. The transfer function* $H(\omega)$ *is plotted as a function of the frequency. The start of the curves corresponds to a wavenumber of* $12821\,\mathrm{cm}^{-1}$ *and with increasing frequency the curves are traversed counterclockwise until* $13300\mathrm{cm}^{-1}$ *is reached. Although the curves have a counterclockwise direction locally, from the origin the direction can be clockwise, meaning a negative phase derivative* ϕ'*. For example, the curve ending at* $-1-2i$ *starts at* $-0.4-1.1i$ *and the phase decreases until* $-1-0.7i$ *is reached. After this point the phase starts to increase again. For thicker samples negative delay times are less common and are related to loops in the curves, like the curve near* $-1.3+0.4i$*. Finally, it can be seen that the curves are not centered around the origin. This means that a contribution of the coherent beam is present.*

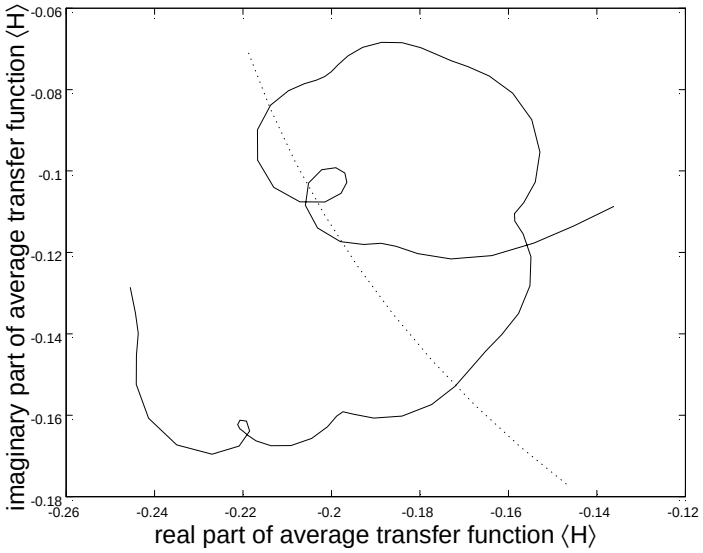

Figure 5.9: Average transfer function of the $1.5\,\mu$m *thick sample. This curve is the average of the curves in Figure 5.8. The dotted line is the theoretical curve for* $n_{eff} = 1.34$ *if only a coherent beam would be present. Clearly this is not the case so it can be concluded that there still is a contribution of incoherent propagation. The contribution of the coherent beam, however, is large enough to completely displace the curve from the origin. The direction of this displacement is used to find the phase velocity. If more measurements are performed, the incoherent contribution should average out better and the average transfer function should converge to the theoretical curve.*

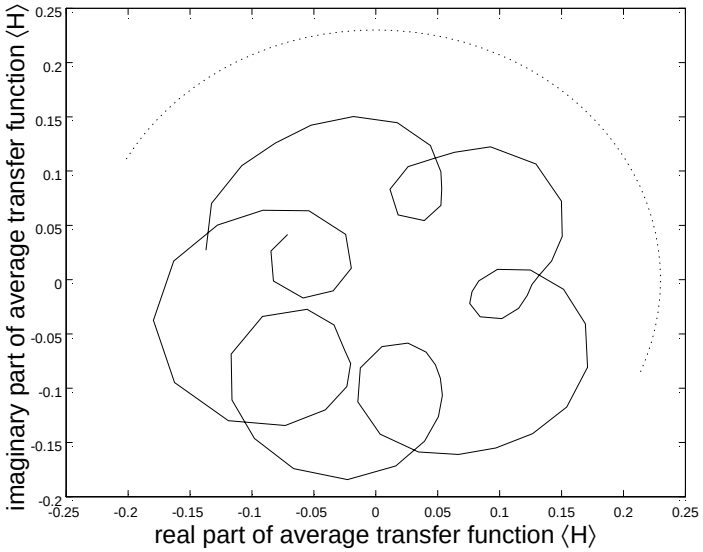

Figure 5.10: The average transfer function of the $8.2\,\mu$m *sample is centered around zero. A fast and a slow rotation are recognized in the curve. The slow rotation corresponds to a time of* 0.16 ps*, the fast rotation corresponds to a delay of* 1.07 ps*. Neither one of these times corresponds to the diffuse traversal time of* 0.56 ps *or the expected coherent phase delay (dotted line). The cause of this effect is unclear, but it might be caused by a misalignment of the setup causing undesired oscillations in the signal.*

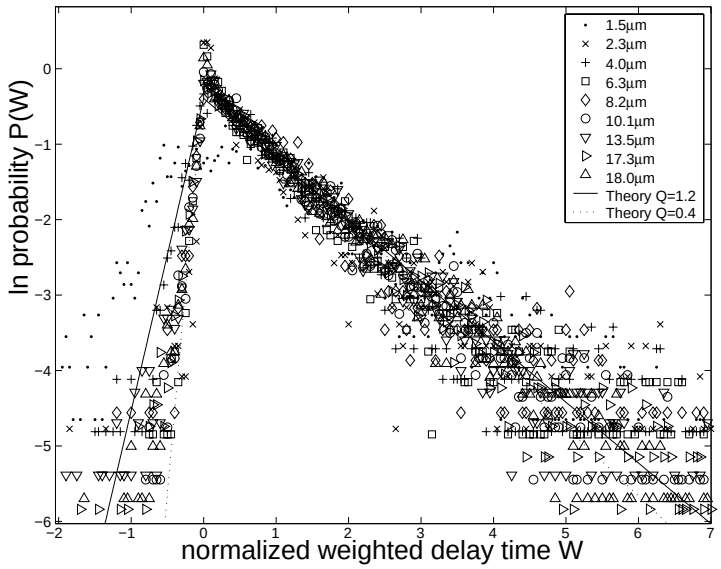

Figure 5.11: Probability distribution of the weighted delay time. All samples produce approximately the same shape, except for the thinnest sample of 1.5 μm *where the top is flattened.*

surements. First this data will be analyzed for a possible time offset introduced by the measurement technique. After this, the dimensionless parameter Q will be extracted from the measurement and the curves will be compared to theory. Finally abnormalities in the shape of the $P(W)$ distribution around $W = 0$ will be analyzed.

5.4.1 Distribution of the weighted delay time

The distributions of the weighted delay time are plotted in Figure 5.11. For all samples except the thinnest one the triangular trend is very clear. First the top of the triangle is examined. This part of the figure is shown enlarged in Figure 5.12. Theoretically the top should be at 0, regardless of sample thickness, mean free path, diffusion constant, extrapolation length or absorption. An offset in determining the delay time can, however, cause the top to be displaced. Instead of $W = \phi'|H(\omega)|^2$ a value of $W_{\text{meas}} = (\phi' + t_0)|H(\omega)|^2$ will be found, causing the whole distribution to shift a bit. Careful examination of the distributions shows that the offset cannot be larger than 5% of $\langle W \rangle$. Assuming that the error in determining $t = 0$ is independent of the sample thickness, $\langle W \rangle$ can be measured with an accuracy of 0.02 ps.

A closer examination of the top of the curves shows that the top of some curves is sharper and higher than expected. This effect is clearly visible for the 2.3 μm, the 6.3 μm and the 18μm samples. A possible explanation for this can be found looking at the separate measurements. It appears that for these samples one or two of the measurements have a cross-correlate that is below the noise level. A measurement containing no cross-correlate but just noise has a low intensity and a random phase delay. In the $P(W)$ distribution this corresponds to a sharp peak around $W = 0$ therefore resulting in a deviation as was seen. Removing a single 'empty' measurement out of the 33 measurements performed on the 18 μm sample caused the curve of this sample to follow the theoretical triangle exactly,

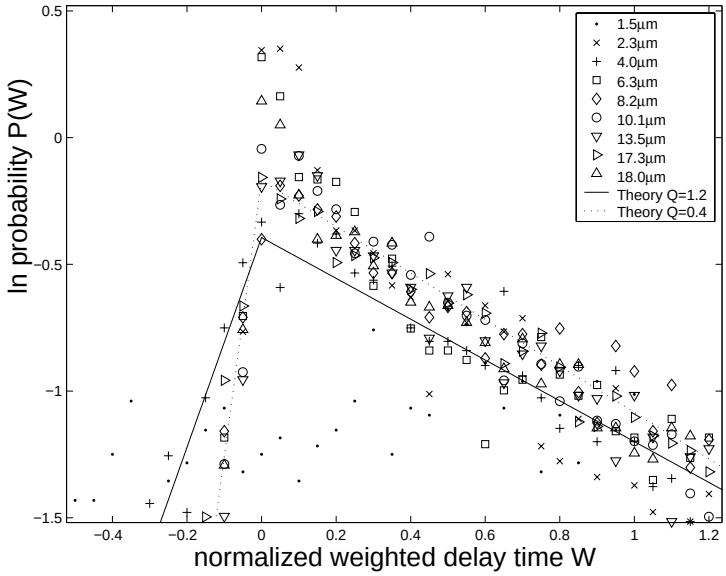

Figure 5.12: Detail of the probability distribution of the weighted delay time. It can be seen that the top of the distribution is at $W = 0$ for all samples, indicating no delay time. Furthermore, the peak is sharper than expected for the 2.3 μm*, the* 6.3 μm *and the* 18.0 μm *samples.*

indicating that this indeed was the cause of this deviation.

Apart from noise, the coherent beam can be responsible for a distortion of the $P(W)$ distribution. This might be the reason that the distribution for the 1.5 μm thick sample is flattened.

5.4.2 Distribution of the delay time

The measured distributions of the delay time ϕ' are shown in Figure 5.13. All samples except for the two thinnest produce distributions that fit well with the theoretical shape of the curve, a manual fit shows that the Q values are between 0.4 and 1.2 (for the 4 μm sample). Values for Q will be calculated from the measurements later in this section. The deviating curves belonging to the two thinnest samples suggest that these measurements are affected by the coherent.

To see how well the data corresponds to Gaussian statistics, the asymmetry $s \equiv (\langle\phi'\rangle - \phi'_{\mathrm{med}})/\langle\phi'\rangle$ of the distributions is calculated. Several mechanisms can cause the statistics to be non-Gaussian. One of these is an inhomogeneous thickness. If the sample thickness is not equal at all positions of the sample, this will cause the probability distribution of ϕ' to be asymmetrical. This effect is likely to be larger for thin samples. Measurements at a thick part of the sample has a broader probability distribution with a higher average value. A combination of measurements on different thicknesses causes the median to be lower than the average value, yielding a positive asymmetry.

A different cause of asymmetry is found if the time window of the measurement is finite, the highest values of the delay time are clipped. This effect can cause an asymmetry in the thickest samples. Clipping removes a few of the highest values and therefore decreases the average value more than the median, causing a negative asymmetry. Finally, a coherent

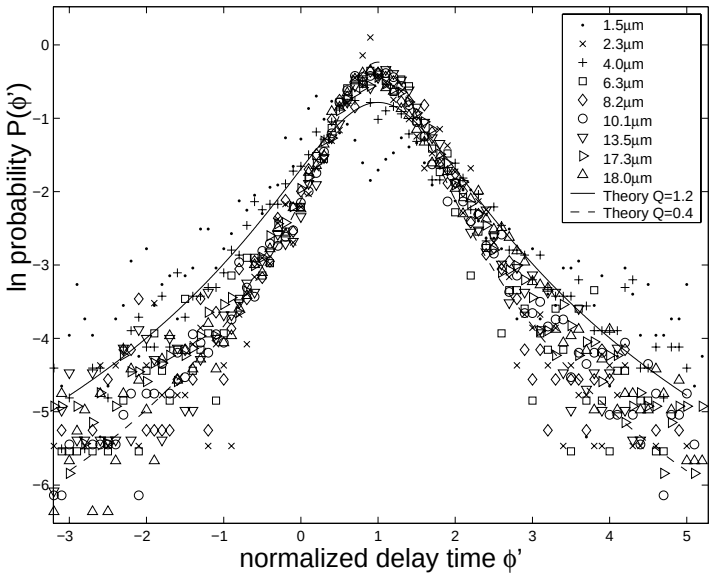

Figure 5.13: Probability distribution of the normalized delay time. The width of the distribution (determined by the Q parameter) depends on the thickness of the sample. In agreement with Eq. (A.34)*, Q is larger for thinner samples. For all samples except the two thinnest ones the probability density curve matches the shape predicted by Eq.* (3.45)*.*

beam could cause an asymmetry in the distribution.

The measured asymmetry is plotted in Figure 5.14. The higher asymmetry in the thinnest samples can be the result of the coherent beam coming trough, but can also be caused by an inhomogeneous thickness. In the 13.5 μm thick sample the effect of a finite time windows is visible, the two thickest samples do not show this effect since a longer measurement range was used.

Finally the methods described in Table 4.2 are used to calculate Q. The theoretical value from equation A.34 is also plotted, together with theoretical curves for ejection depths of 0 and $\frac{2}{3}\ell$. These curves seem to fit the experimental data quite well, but more measurements on samples with a thickness lower than 6 μm are required. It can be seen that all three methods used to calculate Q give approximately the same results, except for the thinnest sample where the deviation from Gaussian statistics is the strongest.

5.4.3 Summary

TiO_2 powder samples with thicknesses between 1.5 μm and 18 μm were investigated by stationary and dynamic transmission measurements. From stationary total transmission measurements the mean free path of $\ell = 0.97$ μm was extracted.

Dynamic measurements showed that the diffuse traversal time obtained from intensity measurements is in good agreement with the delay time obtained from phase measurements, validating the statistics developed in [18]. The time obtained from the fit of the exponential decay of the intensity was corrected for edge effects; the size of these corrections agreed well with the prediction in Eq.(3.25), thus supporting this newly developed theory. The accuracy, however, was not high enough to be conclusive about the value of

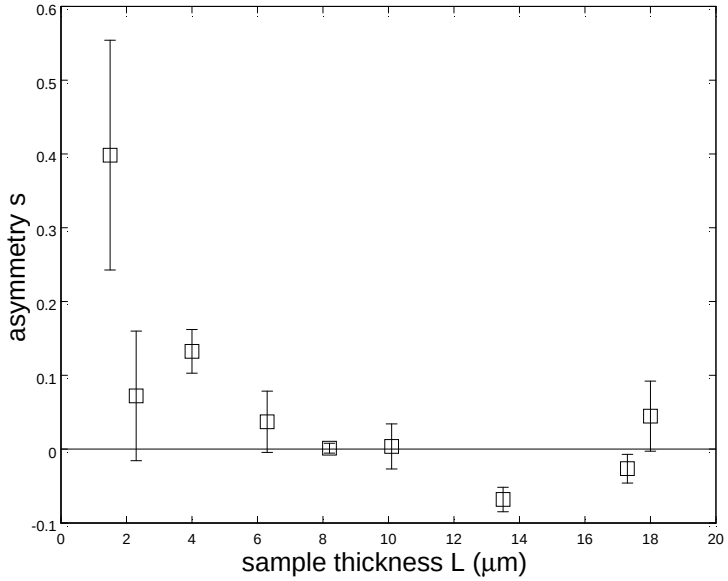

Figure 5.14: Asymmetry as a function of sample thickness. Asymmetry can be caused by the coherent beam, by a varying thickness in a single sample or by the finite time window. The errorbars are obtained by calculating the asymmetry for the first and last half of the measurements separately and comparing the results to the asymmetry found from all measurements. The errorbars are indicative for the statistical error in the determination of the asymmetry.

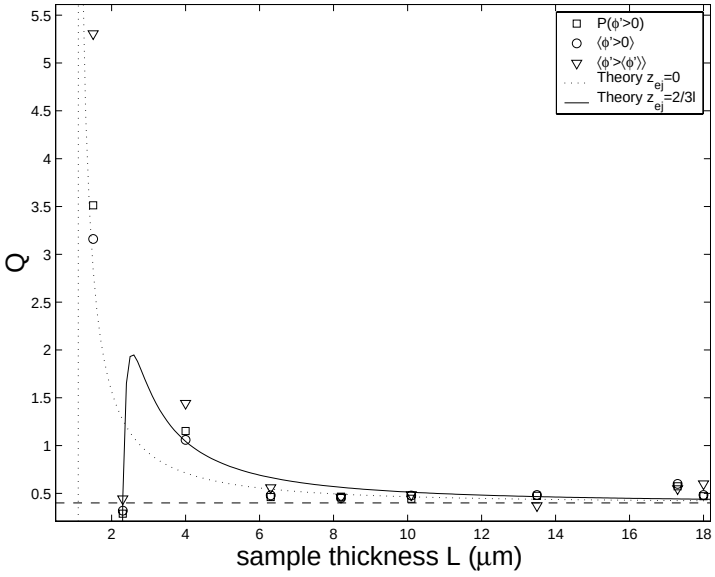

Figure 5.15: Dimensionless parameter Q as a function of sample thickness extracted from the measurement in three different ways as explained in Section 4.4.7. The theoretical value of Q, including the correction for edge effects as was proposed in Appendix 3.4.2*, is shown with a dotted line (the case where $z_{ej} = 0$) and a solid line (the case where $z_{ej} = 2\ell/3$). Although the data is not conclusive as to what is the value of z_{ej}, the values significantly deviate from 0.4 predicted in [18]. It is not clear if the decrease of Q predicted for thinner samples is real or that it is because the theory is no longer valid in this regime.*

the ejection depth z_{ej}.

The square root of the measured traversal time was used to extract the diffusion constant. The values obtained from the fit of the intensity time tail do not depend on the ejection depth and yielded $D = 24.6\,\mathrm{m^2 s^{-1}}$. Determination of the diffusion constant from the other measurements proved difficult since they depend strongly on the edge effect corrections. Values of $D = 28.0\,\mathrm{m^2 s^{-1}}$ to $D = 33.6\,\mathrm{m^2 s^{-1}}$ were found.

The most accurate method of measuring the diffuse traversal time is by calculating the average delay time; which is independent of errors in the amplitude and not hampered by a limited time resolution. Methods using the time resolved intensity are less accurate since the finite bandwidth of the source pulse limits the time resolution.

Analysis of the statistical properties of the phase and the intensity revealed that the thinnest sample has a significant contribution of coherent transmission. The coherent phase velocity in this sample can be measured, yielding $n_{\mathrm{eff}} = 1.34$.

Analysis of the phase statistics showed good agreement with the expected probability functions. The top of $P(W)$ was used to estimate a maximum value for the time offset ($|t_0| < 0.02\,\mathrm{ps}$). A distortion of the peak of $P(W)$ was seen and for some samples it was identified with erroneous measurements.

The asymmetry $P(\phi')$ distribution was used to examine deviations from Gaussian statistics and showed a large deviation for the four thinnest samples, probably caused by coherent transmission or inhomogeneous sample thickness.

It can be concluded that since the four methods of measuring the diffuse traversal time give equal results, the theory is consistent and the data processing is performed correctly. This comparison of measurement methods has not been performed before and supports the theory for edge effect corrections to the traversal time that was developed in Section 3.4.2.

Chapter 6

Conclusion

The propagation of light through disordered materials proved to be a rich and intriguing subject. In the quest for Anderson localization of light, special materials are created to manipulate the propagation of light as strongly as possible. A technique to perform dynamic measurements on light propagating through these media was studied in this thesis. This technique can be used to characterize samples, to study the dynamics of diffusion of light and to identify possible Anderson localization of light.

In the first part of the thesis, existing theory was summarized to find experimentally testable predictions for the propagation of light through random media. This summary included a recent theory describing the statistics of the diffuse delay time [18]. This theory was extended to include edge effects in transmission.

From the theoretical analysis in Chapter 3 it became clear that the diffuse traversal time is a parameter that connects diffusion theory to the delay time statistics. Four independent methods were found to extract this parameter from the same set of measurements. This allowed a comparison of these methods and was a check of the consistency of the theory and the correctness of data acquisition and processing. Measurements showed an excellent agreement between the diffuse traversal time extracted from the measured intensity and the values extracted from the phase statistics. This proved the consistency of the phase statistics and the correctness of the data acquisition and processing. A different method uses a fit of the time tail of the transmitted pulse to find the diffuse traversal time. The results of this measurement support the suggested correction to include edge effects in the phase statistics. Unfortunately, the edge effects could not be measured with enough accuracy to extract physical parameters such as the ejection depth.

A different parameter that is of importance in the description of delay time statistics is the dimensionless parameter Q. We showed that in transmission this parameter is not constant as was assumed before, but depends on the thickness of the sample. A comparison of the measured values of Q to the theoretical predictions showed a good agreement for samples that were thicker than a few mean free paths. For thinner samples, however, the calculated values are more sensitive to errors in the estimated reflection at the boundaries. Not enough samples were measured to validate the theory in this region.

Since the delay time statistics relies on a Gaussian distribution of the light leaving the random medium, this assumption was checked in different ways. Analysis of the intensity and phase distributions showed a deviation from Gaussian statistics in the thinnest

samples. In the thinnest sample of 1.5 μm the coherently propagating beam was identified and the phase velocity in the random medium was extracted from this measurement. The coherent beam caused a deviation from Gaussian statistics, but a larger effect might be due to samples not having the same thickness everywhere. Apart from this effect, deviations due to small holes in the sample were identified by examining the weighted delay time distribution; these deviations could be corrected by removing the corresponding measurements from the set of data.

The setup that was used to perform these measurements is extremely versatile, but a careful processing of the data is required since artefacts are introduced easily. Especially in the calculation of the phase derivative and in filtering the data special care has to be taken. The setup in principle has a time resolution of 0.26 fs but when time resolved intensity is measured, the resolution is limited to 0.1 ps due to the finite bandwidth of the source; this fact was not taken into account in earlier experiments using this setup [14, 21]. This resolution was achieved using a Chebychev filter to remove noise outside the source bandwidth; less careful filtering can seriously distort the measurements.

An important problem of the measurement technique is that it is difficult to determine the time origin. If the samples are on a substrate the delay inside the substrate has to be compensated for. Since the setup was improved to allow measuring reflected light, this feature could be used to measure the time difference between the reflection from the front and the back of the substrate, thus allowing a very accurate determination of the substrate thickness. By examining the phase statistics, it was proven that no time offset was present after compensation. Since the maximum of this distribution is at the time origin, this method can in principle be used to determine this origin.

Despite the high time resolution, accurate time origin and a dynamic range of 60dB, the uncertainty in determining the diffuse delay time or other parameters is a few percents. The most important limitation is the statistical error; the quantities that are measured are different for every single measurement. To determine their average values more accurately, more measurements have to be performed.

6.1 Suggestions for improvement

Although the setup allows very sensitive and detailed measurement of the transmitted light, some improvements could make the setup more flexible and even more sensitive. Two restrictions of the current setup are that the frequency and the angle of the detector are fixed. It would be very advantageous to be able to scan the frequency of the probe light. Not only would this overcome the problem of the limited bandwidth, it would also allow a frequency dependent scan of important parameters like the diffusion constant. This way the regime with the strongest scattering can be selected, increasing the chance of observing localization. A variable detector angle could resolve angular correlations in time and in reflection it allows a study of the dynamics of the enhanced backscatter cone (the delay time statistics in the localizing regime was predicted to be qualitatively different from the statistics in the diffuse regime [36]). Furthermore, it will be possible to selectively exclude or include the coherent beam in order to compare the resulting signals.

Further improvements can be made to improve the dynamic range. The signal power can be increased by using more of the light of the pulsed laser. At the moment 50mW

of laser light is used, but this amount can probably be increased without damaging the sample. Furthermore, a large fraction of the light is lost in the BioRad. A setup where only the reference beam passes through the BioRad could be used. Since this beam is strong enough, this would eliminate the problem. The dynamic range is further limited by unwanted reflections which cause extra cross-correlates. These reflections should be eliminated, possibly by using a different detector.

The time offset accuracy can be improved by using samples without substrate or manufacture the samples in such a way that the substrate is not completely covered. If a part of the substrate is not covered it can be used to perform the reference measurement on. This way the reference measurement includes the delay caused by the substrate and no further compensation for the substrate is needed.

Finally a careful study of the electronic noise in the system has to be made in order to determine what factor limits the dynamic range. Using a chopper and a lock-in amplifier will probably yield little improvement since the signal is already filtered with a very sharp bandpass filter during the data processing.

6.2 Future work

Because of the countless possibilities of the setup, there is a lot that still can be done. Without altering the setup, light reflected off disordered samples can be investigated. The same statistical analysis can be performed as for transmitted light, but different physical parameters are obtained. These measurements have been performed on strongly scattering samples [21], but the theoretical explanation is not always satisfactory. A careful re-examination of the treatment of boundaries and the use of less strongly scattering reference samples will probably answer many questions.

Of course it would be very interesting to perform the same measurements as described in this thesis on extremely strongly scattering media. Now the method is well understood, it is feasible to look for deviations from classical diffusion theory in these samples. If thinner samples are used, the edge effects have to be taken into account properly. Since the corrections in this thesis use simplified boundary conditions and do not take into account absorption, a better theoretical understanding of these effects is desired.

With the suggested improvements even more measurements become possible and a full characterization of a sample could be within reach. Since the statistical error can only be reduced by performing more measurements, the amount of measurements could quickly become unmanageable, especially if the angle or frequency is scanned. If a solution to this final problem is found, all information that can possibly be obtained from far field measurements can be found with this setup.

Appendix A

Derivations

A.1 Transforming the Green function

In this section, the bare Green function $g(\mathbf{p})$ will be transformed to real space coordinates. The integral that needs to be evaluated is:

$$g(\mathbf{r}) = \frac{1}{(2\pi)^3} \int d\mathbf{p} g(\mathbf{p}) e^{i\mathbf{r}\cdot\mathbf{p}} \tag{A.1}$$

To solve this integral, first spherical coordinates are defined and the integration over the angular parameters is done. Finally the integration over the radius is evaluated using contour integration. At the end of the section an one-dimensional Fourier transform is used to calculate a plane wave solution from the Green function.

A.1.1 Spherical coordinates

Spherical coordinates are introduced for $\mathbf{p}$. The positive z axis is chosen to be parallel to $\mathbf{r}$. Therefore $\mathbf{r}\cdot\mathbf{p} = rp\cos\theta$ and Eq. (A.1) can be written:

$$g(\mathbf{r}) = \frac{1}{(2\pi)^3} \int_0^\infty \int_0^\pi \int_0^{2\pi} d\phi d\theta dp \frac{1}{p^2 - k^2} e^{irp\cos\theta} p^2 \sin\theta \tag{A.2}$$

The integration over ϕ is trivial. θ is substituted by $\mu = \cos\theta$, and $d\theta$ by $-d\mu/\sin\theta$.

$$g(\mathbf{r}) = \frac{-1}{(2\pi)^2} \int_0^\infty \int_1^{-1} d\mu dp \frac{1}{p^2 - k^2} e^{irp\mu} p^2 \tag{A.3}$$

$$\begin{aligned} g(\mathbf{r}) &= \frac{-1}{(2\pi)^2} \frac{1}{ir} \int_0^\infty dp \frac{1}{p^2 - k^2} \frac{e^{-irp} - e^{irp}}{p} p^2 \\ &= \frac{1}{(2\pi)^2} \frac{1}{ir} \int_{-\infty}^\infty dp \frac{p e^{irp}}{p^2 - k^2} \end{aligned} \tag{A.4}$$

The integral in (A.4) is undefined due to the divergence at $p = k$. If an arbitrarily small offset is added to the denominator, however, the integral can be evaluated using contour integration.

A.1.2 Contour integration

The residue theorem states that the integral of a function $f(p)$ over a closed contour C equals the sum of the residues inside the contour:

$$\oint_C dp f(p) = 2\pi i \sum (\text{residues in C}) \tag{A.5}$$

The residues can be found by making a Laurent series expansion of $f(p)$ around its poles p_0:

$$f(p) = \sum_{n=-\infty}^{\infty} a_n (p - p_0)^n \tag{A.6}$$

Coefficient a_{-1} is called the residue.

By defining a convenient contour, the integral in Eq. (A.4) can be evaluated. We choose the contour to be a closed semicircle in the positive imaginary part of the complex plane. Using the residue theorem we have:

$$\int_{-R}^{R} dp f(p) + \int_{0}^{\pi} d\phi f(Re^{i\phi}) = 2\pi i \sum (\text{residues in } C) \tag{A.7}$$

The first term describes the straight part of the contour. In the limit $R \to \infty$, it equals the integral we want to evaluate. The second term describes integration over the semicircle. The integrand equals:

$$\frac{Re^{i\phi} e^{ir(Re^{i\phi})}}{(Re^{i\phi})^2 - k^2} \tag{A.8}$$

Because $0 \leq \phi \leq \pi$, the exponential has a negative real part for $r > 0$ and is zero in the limit $R \to \infty$. If $r = 0$, the integrand also vanishes for large R. This means that the second term in Eq. (A.7) is zero. Therefore the first part, which is the integral we are interested in, is equal to the sum over the residues in C.

To find the residues, the poles of $g(p)$ inside the contour have to be expanded. This poses a problem since the poles of $g(p)$ are on the real axis, so they are exactly on contour C. To fix this, a small offset ($i2\epsilon k$) is added to the denominator of $g(p)$. Neglecting the term of order ϵ^2, g now has poles at $p = -k - i\epsilon$ and at $p = k + i\epsilon$. Only the second pole is in the contour. Therefore:

$$g(\mathbf{r}) = \frac{1}{(2\pi)^2} \frac{1}{ir} \int_{-\infty}^{\infty} dp \frac{pe^{irp}}{(p + k + i\epsilon)(p - k - i\epsilon)} = \frac{1}{2\pi r} \frac{(k + i\epsilon) e^{ir(k+i\epsilon)}}{2(k + i\epsilon)} \tag{A.9}$$

Taking the limit $\epsilon \downarrow 0$ gives the final result:

$$g(\mathbf{r}) = -\frac{e^{ikr}}{4\pi r} \tag{A.10}$$

A.2 Regularization of the Green function

In the point scattering model, scatterers are treated as point sources. The field emitted by a point source is described by the Green function, but this function has a discontinuity at $r = 0$. Due to this discontinuity it is not possible to know or to estimate the returning propagator for light scattered from a particle.

To solve this problem, the divergence of the Green function has to be fixed. This is done by introducing a regularized Green function $\tilde{g}(\mathbf{r})$. There are many ways of performing the regularization. The exact value of $\tilde{g}(0)$ depends on the type of regularization and the choice of regularization parameters.

Two types of regularizations are described. First a regularization in real space is used, then the regularization is performed in wave-vector space.

A.2.1 Regularization with a spherical source

This regularization method replaces the point source in the definition of the Green function from Eq. (2.2) by a small spherical source with radius a. The phase inside the source is assumed to be constant, which can only be approximately true if $a \ll 1/k$. Solving this equation yields $\tilde{g}(\mathbf{r})$.

$$\nabla^2 \tilde{g}(\mathbf{r}, \mathbf{r}') - k^2 \tilde{g}(\mathbf{r}, \mathbf{r}') = \begin{cases} \frac{1}{\frac{4}{3}\pi a^3} & \text{for } |\mathbf{r} - \mathbf{r}'| \leq a \\ 0 & \text{for } |\mathbf{r} - \mathbf{r}'| > a \end{cases} \tag{A.11}$$

This definition gives a finite result for $\tilde{g}(0)$ that depends on the radius of the source. In far field ($r \gg a$) in the limit $a \ll 1/k$ (small scatterer) the results will be the same as for point scatterers.

The value of $\tilde{g}(0)$ can be found by integrating $g(\mathbf{r})$ over the spherical source:

$$\begin{aligned} \tilde{g}(0) &= \frac{3}{4\pi a^3} \int_{r \leq a} d\mathbf{r} \frac{e^{ikr}}{4\pi r} \\ &= \frac{3}{4\pi a^3} \int_0^a dr \frac{e^{ikr}}{r} r^2 \\ &= \frac{3}{4\pi a^3} \left[\frac{a e^{ika}}{ik} + \frac{e^{ika}}{k^2} - \frac{1}{k^2} \right] \end{aligned} \tag{A.12}$$

To find $\tilde{g}(0)$ for a small scatterer ($a \ll 1/k$), the exponentials are expanded:

$$\begin{aligned} \tilde{g}(\mathbf{r}) &= \frac{3}{4\pi a^3} \left[\frac{-ika - (ika)^2 - \frac{1}{2}(ika)^3}{k^2} + \frac{1 + ika + \frac{1}{2}(ika)^2 + \frac{1}{6}(ika)^3}{k^2} - \frac{1}{k^2} \right] \\ &= \frac{3}{4\pi a^3} \left[\frac{\frac{1}{2}(ka)^2 + \frac{1}{3} i (ka^3)}{k^2} \right] \\ &= \frac{\Lambda}{4\pi} + \frac{ik}{4\pi} \end{aligned} \tag{A.13}$$

For this method $1/\Lambda = \frac{2}{3}a$. A different method, based on the resonance frequency of a Mie sphere, gives $1/\Lambda = 0.822a$.

A.2.2 Regularization in wave-vector space

A different approach uses a cutoff in wavevector space. It removes components that oscillate on a smaller scale than the size of the scatterer ($\sim 1/\Lambda$). The regularized Green function can be defined:

$$\tilde{g}(\mathbf{p}) = \frac{\Lambda}{\Lambda + p^2} \frac{1}{p^2 - k^2} \tag{A.14}$$

Fourier transforming this function is similar to the transform described in section A.1. The only difference is that in the contour integration four poles are present instead of one (compare Eq. (A.9)).

$$\tilde{g}(\mathbf{r}) = \frac{1}{(2\pi)^2} \frac{1}{ir} \int_{-\infty}^{\infty} dp \frac{\Lambda^2 p e^{irp}}{(p + i\Lambda)(p - i\Lambda)(p + k + i\epsilon)(p - k - i\epsilon)} \tag{A.15}$$

For a contour in the positive imaginary part of the complex plane, only the poles at $p = i\Lambda$ and $p = k + i\epsilon$ contribute:

$$\begin{aligned}
\tilde{g}(\mathbf{r}) &= \frac{1}{2\pi r} \left[\frac{i\Lambda^3 e^{-\Lambda r}}{2i\Lambda(i\Lambda + k + i\epsilon)(i\Lambda - k - i\epsilon)} + \frac{\Lambda^2 (k + i\epsilon) e^{i(k+i\epsilon)r}}{(k + i\epsilon + i\Lambda)(k + i\epsilon - i\Lambda) 2(k + i\epsilon)} \right] \\
&= \frac{1}{4\pi r} \left[\frac{\Lambda^2 e^{-\Lambda r}}{-\Lambda^2 - k^2} + \frac{\Lambda^2 e^{ikr}}{\Lambda^2 + k^2} \right] \\
&= \frac{\Lambda^2}{\Lambda^2 + k^2} \frac{e^{ikr} - e^{-\Lambda r}}{4\pi r}
\end{aligned} \tag{A.16}$$

An expansion around $r = 0$ gives the same result as in the previous section if $\Lambda \gg k$:

$$\begin{aligned}
\tilde{g}(0) &= \frac{\Lambda^2}{\Lambda^2 + k^2} \lim_{r \to 0} \frac{(1 + ikr) - (1 - \Lambda r)}{4\pi r} \\
&\approx \frac{\Lambda}{4\pi} + \frac{ik}{4\pi}
\end{aligned} \tag{A.17}$$

In this method, Λ is a free parameter. The previous section showed a relation between Λ and the inverse scatterer size. Eq. (A.14) shows that the regularization acts as a low pass filter, cutting off high spatial components with $p > \Lambda$. Small scatterers (high Λ) can have quickly oscillating components, whereas scatterers with a larger radius (low Λ) will only contain slower oscillating components. Λ has to be larger than k in order not to cut off propagating modes.

A.3 Diffusion in finite media

In the whole derivation of the diffusion equation (3.22), an infinite medium was assumed. Extending the theory to include finite random materials or materials with a varying mean free path would mean a serious complication from the very start of the derivation of the diffusion equation. For this reason a different approach is used to handle boundaries. This method assumes Eq. (3.22) is valid everywhere in the medium and uses appropriate boundary conditions at the material surfaces.

To find these boundary conditions, the concept of flux is introduced. Flux is the amount of electromagnetical intensity moving through a unit surface per second. The flux in a certain direction equals the product of the intensity moving in that direction and the average velocity. Assuming that the average energy velocity equals v_e, the flux in direction $\mathbf{s}$ at position $\mathbf{r}$ equals $J(\mathbf{s}, \mathbf{r}) = v_e I(\mathbf{s}, \mathbf{r})$. The value $I(\mathbf{s}, \mathbf{r})$ is called the specific intensity and represents the intensity corresponding to flux in direction s. Integrating over all directions gives the total intensity,

$$I(\mathbf{r}) = \frac{1}{v_e} \int_0^{2\pi} \int_0^{\pi} d\theta d\phi \sin\theta J(\mathbf{s}, \mathbf{r}), \tag{A.18}$$

where $s = (\cos\phi \sin\theta, \sin\phi \sin\theta, \cos\theta)$. A second relation between the intensity and the flux is found from energy conservation; the difference between flux flowing into a certain volume and the outgoing flux has to equal the change in intensity,

$$\nabla \mathbf{J} = -\frac{dI}{dt}, \tag{A.19}$$

where the nett flux $\mathbf{J}$ is the vector sum of all fluxes. Combining this with Eq. (3.22) gives,

$$\mathbf{J} = -D\nabla I \tag{A.20}$$

The nett flux can be found by summing the fluxes in all directions taking into account their directions,

$$\mathbf{J} = \int_0^{2\pi} \int_0^{\pi} d\theta d\phi \sin\theta J(\mathbf{s}, \mathbf{r})\mathbf{s} \tag{A.21}$$

These relations can be used to find boundary conditions for the diffusion equation. We investigate a slab of a diffusive material. It is assumed that the outgoing flux is distributed uniformly so that $J(\mathbf{s}, \mathbf{r}) = J_{\text{out}}/(2\pi)$ for all outgoing angles. Part of the outgoing flux is reflected at the sample boundary and causes an incoming flux. Assuming the incoming flux also has a uniform distribution over all angles, $J(\mathbf{s}, \mathbf{r}) = RJ_{\text{out}}/(2\pi)$ for all incoming angles. A value for the reflection coefficient R can be found integrating the Fresnel reflection coefficient over all angles. Now we can calculate the intensity and the nett flux to find the boundary conditions,

$$I(\mathbf{r}) = \frac{1}{v_\mathrm{e}} J_\mathrm{out}[1+R] \tag{A.22}$$

$$\begin{aligned}\nabla I &= \frac{1}{D}\int_0^{2\pi} d\phi J_\mathrm{out}\left[\int_0^{\frac{\pi}{2}} d\theta \sin\theta \mathbf{s} + \int_{\frac{\pi}{2}}^{\pi} d\theta \sin\theta R\mathbf{s}\right] \\ &= \frac{1}{2D} J_\mathrm{out}[1-R]\mathbf{e_z}\end{aligned} \tag{A.23}$$

Combining these two relations finally yields the boundary condition,

$$\frac{I(\mathbf{r})}{z_e}\Big|_{z=0^+} - \frac{dI(\mathbf{r})}{dz}\Big|_{z=0^+} = 0, \tag{A.24}$$

where $z_e \equiv (2D[1+R])/(v_\mathrm{e}[1-R]) = \frac{2}{3}\ell(1+R)/(1-R)$ is called the extrapolation length (see also [37, 38]. A linear expansion of this boundary condition gives $I(-z_{e1}) = 0$ for the left boundary and $I(L+z_{e2}) = 0$ for the right boundary. With these modified boundary conditions a set of eigenmodes of the form $\sin((z+z_{e1})/L'n\pi)$ is found, where $L' \equiv L + z_{e1} + z_{e2}$.

A.3.1 Transmission through a slab

A beam of light incident on a random sample does not give rise to a diffuse intensity immediately, but is directional as long as it is not scattered. Therefore we can approximate the effect of an incoming beam by a source of diffuse intensity at $z = \ell$ [39, 23, 9]. Furthermore, it has been suggested that to calculate the outgoing flux, it is not correct to calculate J at $z = L$ since light leaving the sample has traveled the last part ballistically and originates from one mean free path in the sample. Therefore the transmitted flux is calculated at a position $z = L - z_\mathrm{ej}$, where $z_\mathrm{ej} = \ell$ [23, 28] or $z_\mathrm{ej} = \frac{2}{3}\ell$ [9]. It can, however, be argued that $z_\mathrm{ej} = 0$, because coherent and unscattered propagation is also included in the intensity propagator R (3.21). For the moment, we just refer to this value as z_ej.

First the field is expanded in eigenmodes,

$$I(z,t) = \sum_{n=1}^{\infty} \exp\left(\frac{-\pi^2 n^2 Dt}{(L')^2}\right) \sin\left(\frac{z+z_{e1}}{L'}n\pi\right) \frac{\sin\left(\frac{\ell+z_{e1}}{L'}n\pi\right)}{L'}, \tag{A.25}$$

where the first factor comes from Eq. (3.20), the second term is the eigenmode and the last term is the coefficient corresponding to the expansion of the delta source in eigenmodes. The flux is calculated by applying (A.20) at $z = L - z_\mathrm{ej}$,

$$J_T = -D\sum_{n=1}^{n} \exp\left(\frac{-\pi^2 n^2 Dt}{(L')^2}\right) \frac{n\pi}{L'} \cos\left(\frac{L - z_\mathrm{ej} + z_{e1}}{L'}n\pi\right) \frac{\sin\left(\frac{\ell+z_{e1}}{L'}n\pi\right)}{L'}. \tag{A.26}$$

This equation is of experimental importance, since it gives the time resolved measured intensity. For large t, only the terms with $n = 1$ survive, decaying exponentially with

a slope of $-\pi^2 D/L'$. Therefore fitting the time tail of the intensity transfer gives the diffusion constant.

Several other interesting parameters will be extracted from this equation, including the average intensity and an approximation of the correlation function. First the equation is rewritten using the trigonometric identity $2\cos(a)\sin(b) = \sin(a+b) - \sin(a-b)$,

$$J_T = -\frac{\pi D}{2(L')^2} \sum_{n=1}^{\infty} \exp\left(\frac{-\pi^2 n^2 D t}{(L')^2}\right) \left[\sin(\alpha n\pi) - \sin(\kappa n\pi))\right], \tag{A.27}$$

with $\alpha \equiv (L + 2z_{e1} + \ell - z_{\mathrm{ej}})/L'$ and $\kappa \equiv (L - \ell - z_{\mathrm{ej}})/L'$. We conclude that α represents the asymmetry of the system; if the light is entering the sample at the same depth as at which it is ejected ($\ell = z_{\mathrm{ej}}$) and both extrapolation lengths are equal ($z_{e1} = z_{e2}$), the system is symmetrical and $\sin n\alpha\pi = 0$. The parameter κ equals the distance between the source plane and the ejection plane, divided by the total thickness of the system including extrapolations. For an infinite slab thickness this ratio equals unity and $\sin(\kappa n\pi) \to 0$. We can say that κ represents the effect of the finite slab thickness.

Total transmission

The total nett flux that is transmitted is found by integrating Eq.(A.27) over t.

$$\begin{aligned}\int dt J_T &= -\frac{\pi D}{2(L')^2} \sum_{n=1}^{\infty} \frac{(L')^2}{\pi^2 n^2 D} n \left[\sin(\alpha n\pi) - \sin(\kappa n\pi)\right] \\ &= -\frac{1}{2\pi}\left[\frac{\pi}{2}(\kappa - \alpha)\right] \\ &= \frac{\ell + z_{e1}}{2L'}\end{aligned} \tag{A.28}$$

where identity $A.35$ was used to evaluate the infinite series. This equation gives the expected total nett flux transmitted through a slab in the forward direction, not including coherent propagation. If the assumption is made that the flux is spread equally over all outgoing directions, the total flux integrated over all angles equals twice this value.

Diffuse traversal time

A way to characterize the time it takes a pulse to propagate through a slab is to calculate the diffuse traversal time $\tau_d \equiv \left\langle \int dt J_T t \right\rangle / \left\langle \int dt J_T \right\rangle$. In the particle diffusion model this corresponds to calculating the average arrival time of particles that diffused through a slab. The calculation is analogous to the calculation of the total intensity.

$$\begin{aligned}\int dt J_T t &= -\frac{\pi D}{2(L')^2}\sum_{n=1}^{\infty}\frac{L'^4}{\pi^4 n^4 D^2} n\left[\sin(\alpha n\pi)-\sin(\kappa n\pi)\right] \\ &= -\frac{L'^2}{2\pi^3 D}\left[\frac{\pi^3}{6}\alpha-\frac{\pi^3}{4}\alpha^2+\frac{\pi^3}{12}\alpha^3-\frac{\pi^3}{6}\kappa+\frac{\pi^3}{4}\kappa^2-\frac{\pi^3}{12}\kappa^3\right] \\ &= \frac{z_{\ell 1}}{2L'}\left[\frac{L'^2}{6D}-\frac{z_{\ell 1}^2+3z_{\ell 2}^2}{6D}\right], \qquad \text{(A.29)}\end{aligned}$$

$$\tau_d = \frac{L'^2}{6D}-\frac{z_{\ell 1}^2+3z_{\ell 2}^2}{6D}, \qquad \text{(A.30)}$$

where $z_{\ell 1}\equiv z_{e1}+\ell$ and $z_{\ell 1}\equiv z_{e1}+z_{\rm ej}$. For $L'\gg \ell, z_{e1}, z_{e2}$ this amounts to $\tau_d = L'^2/(6D)$, the value that is normally used. This is a very rough approximation however.

Correlation function

The correlation function for the field at the detector is given by the fourier transform of J_T. We will calculate $C(\Omega) = J_T(\Omega)/J_{T0}$ to the second order in Ω since these values are used to calculate the phase statistics (Section 3.5.2 and 3.5.3). Fourier transforming Eq.(A.27) with respect to time gives:

$$J_T(\Omega) = -\frac{\pi D}{2(L')^2}\sum_{n=1}^{\infty}-\frac{n\pi}{n^2\pi^2+i\Omega L'^2/D}\left[\sin(\alpha n\pi)-\sin(\kappa n\pi)\right], \qquad \text{(A.31)}$$

Only an expansion to the second order in Ω is required,

$$J_T(\Omega) = -\sum_{n=1}^{\infty}\left[\frac{1}{2\pi n}+\frac{i\Omega(L')^2/D}{2\pi^3 n^3}+\frac{\Omega^2(L')^4/D^2}{2\pi^5 n^5}\right]\cdot\left[\sin(\alpha n\pi)-\sin(\kappa n\pi)\right]+O(\Omega^3) \qquad \text{(A.32)}$$

The first term can be recognized to be the total forward transmission J_{T0}. The second term equals the diffuse traversal time times J_{T0} and the third term is evaluated using Eq.(A.37). Normalizing gives the field correlation function:

$$C(\Omega) = 1+i\Omega\tau_d+\Omega^2\left[-\frac{7}{10}\tau_d^2+\frac{z_{\ell 1}^4+12z_{\ell 2}^4+3z_{\ell 1}^2z_{\ell 2}^2-(z_{\ell 1}^2+3z_{\ell 2}^2)(L')^2}{90D^2}\right]+O(\Omega^3) \qquad \text{(A.33)}$$

The dimensionless parameter $Q\equiv -2b/a^2-1$ that was introduced in Section 3.5.2, will be affected by edge effects. a equals τ_d and b equals the second factor in Eq. (A.33),

$$Q = \frac{2}{5}-\frac{z_{\ell 1}^4+12z_{\ell 2}^4+3z_{\ell 1}^2z_{\ell 2}^2-(z_{\ell 1}^2+3z_{\ell 2}^2)(L')^2}{45D^2\tau_d^2} \qquad \text{(A.34)}$$

This value is smaller than the value of $\frac{2}{5}$ used in literature [18], especially for thin samples.

A.4 Some series identities

$$\begin{aligned}\sum_{n=1}^{\infty}\frac{\sin(\alpha n\pi)}{n} &= \frac{\pi}{2}\int_{-\alpha}^{\alpha}d\alpha_1\sum_{n=1}^{\infty}\cos(\alpha n\pi)\\ &= \frac{\pi}{2}\int_{-\alpha}^{\alpha}\left[\delta(\alpha)-\frac{1}{2}\right]\\ &= \frac{\pi}{2}(1-\alpha)\end{aligned} \tag{A.35}$$

$$\begin{aligned}\sum_{n=1}^{\infty}\frac{\sin(\alpha n\pi)}{n^3} &= \pi^2\sum_{n=1}^{\infty}\int_0^{\alpha}d\alpha_3\left[\frac{1}{\pi n^2}-\int_0^{\alpha_3}d\alpha_2\frac{\sin(\alpha_2 n\pi)}{n}\right]\\ &= \pi^2\int_0^{\alpha}d\alpha_3\left[\frac{\pi}{6}-\frac{\pi}{2}\int_0^{\alpha_3}d\alpha_2\,(1-a_2)\right]\\ &= \pi^2\int_0^{\alpha}d\alpha_3\left[\frac{\pi}{6}-\frac{\pi}{2}\alpha_3+\frac{\pi}{4}\alpha_3^2\right]\\ &= \frac{\pi^3}{6}\alpha-\frac{\pi^3}{4}\alpha^2+\frac{\pi^3}{12}\alpha^3\end{aligned} \tag{A.36}$$

$$\begin{aligned}\sum_{n=1}^{\infty}\frac{\sin(\alpha n\pi)}{n^3} &= \pi^2\sum_{n=1}^{\infty}\int_0^{\alpha}d\alpha_2\left[\frac{1}{\pi n^4}-\int_0^{\alpha_2}d\alpha_1\frac{\sin(\alpha_1 n\pi)}{n^3}\right]\\ &= \pi^2\int_0^{\alpha}d\alpha_2\left[\frac{\pi^3}{90}-\int_0^{\alpha_2}d\alpha_1\left(\frac{\pi^3}{6}\alpha_1-\frac{\pi^3}{4}\alpha_1^2+\frac{\pi^3}{12}\alpha_1^3\right)\right]\\ &= \pi^2\int_0^{\alpha}d\alpha_2\left[\frac{\pi^3}{90}-\frac{\pi^3}{12}a_2^2+\frac{\pi^3}{12}a_2^3-\frac{\pi^3}{48}a_2^4\right]\\ &= \frac{\pi^5}{90}\alpha-\frac{\pi^5}{36}a^3+\frac{\pi^5}{48}a_2^4-\frac{\pi^5}{240}a_2^5\end{aligned} \tag{A.37}$$

Bibliography

[1] P.W.Anderson, *Absence of Diffusion in Certain Random Lattices*, Physical Review **109**, 1492 (1953).

[2] S. John, *Electromagnetic Absorption in a Disordered Medium near a Photon Mobility Edge*, Physical Review Letters **53**, 2169 (1984).

[3] P. Anderson, *The question of classical localization: a theory of white paint?*, Philosophical Magazine B **52**, 505 (1985).

[4] Y. Kuga and A. Ishimaru, *Retroreflectance from a dense distribution of spherical particles*, Journal of the Optical Society of America **1**, 831 (1984).

[5] M. P. van Albeda and A. Lagendijk, *Opservation of Weak Localization of Light in a Random Medium*, Physical Review Letters **55**, 2692 (1985).

[6] P.-E. Wolf and G. Maret, *Weak Localization and Coherent Backscattering of Photons in Disordered Media*, Physical Review Letters **55**, 2696 (1985).

[7] M. P. van Albeda, M. B. van der Mark, and A. Lagendijk, *Observation of Weak Localization of Light in a Finite Slab: Anisotropy Effect and Light-Path Classification*, Physical Review Letters **58**, 361 (1987).

[8] M. B. van der Mark, M. P. van Albeda, and A. Lagendijk, *Light scattering in strongly scattering media: Multiple scattering and weak localization*, Physical Review B **37**, 3575 (1988).

[9] J. F. de Boer, *Optical fluctuations on the transmission and reflection of mesoscopic systems* (University of Amsterdam, Amsterdam, 1995).

[10] D. S. Wiersma, P. Bartolini, A. Lagendijk, and R. Righini, *Localization of light in a disordered medium*, Nature **390**, 671 (1997).

[11] F. J. P. Schuurmans, M. Megens, D. Vanmaekelbergh, and A. Lagendijk, *Light Scattering near the Localization Transition in Macroporous GaP Networks*, Physical Review Letters **83**, 2183 (1999).

[12] F.Scheffold, R.Lenke, R.Tweer, and G.Maret, *Localization or classical diffusion of light?*, Nature **398**, 206 (1999).

[13] R. H. J. Kop and R. Sprik, *Phase-sensitive interferometry with ultrashort optical pulses*, Review of Scientific Instruments **66**, 5459 (1995).

[14] R. H. Kop, P. de Vries, R. Sprik, and A. Lagendijk, *Observation of Anomalous Transport of Strongly Multiple Scattered Light in Thin Disordered Slabs*, Physical Review Letters **79**, 4389 (1997).

[15] J. G. Rivas, R. Sprik, A. Lagendijk, L. D. Noordam, and C. W. Rella, *Static and dynamic transport of light close to the Anderson localization transition*, Physical Review E **63**, 046613 (2001).

[16] S. Skipetrov and B. van Tiggelen, arXiv:cond-mat/0309381 v1 16 Sep, 2003 (unpublished).

[17] A. Chabanov, Z. Zhang, and A. Genack, *Breakdown of diffusion in dynamics of extended waves in mesoscopic media*, Physical Review Letters **90**, 203903 (2003).

[18] B. van Tiggelen, P. Sebbah, M. Stoytchev, and A. Genack, *Delay-time statistics for diffuse waves*, Physical Review E **59**, 7166 (1999).

[19] P. Sebbah, O. Legrand, and A. Genack, *Fluctuations in photon local delay time and their relation to phase spectra in random media*, Physical Review E **59**, 2406 (1999).

[20] A. Genack, P. Sebbah, M. Stoytchev, and B. van Tiggelen, *Statistics of Wave Dynamics in Random Media*, Physical Review Letters **82**, 715 (1999).

[21] P. M. Johnson, A. Imhof, B. P. Bret, J. G. Rivas, and A. Lagendijk, *Time Resolved Pulse Propagation in a Strongly Scattering Material*, Physical Review E **68**, 016604 (2003).

[22] M. van Rossum and Th.M.Nieuwenhuizen, *Multiple scattering of classical waves*, Review of Modern Physics **71**, 313 (1999).

[23] M. B. van der Mark, *Propagation of light in disordered media: A search for Anderson localization* (University of Amsterdam, Amsterdam, 1990).

[24] H. van de Hulst, *Light Scattering by Small Particles* (Dover Publications, Inc., New York, 1957, 1981).

[25] H. Kwakernaak and R. Sivan, *Modern Signals and Systems* (Prenctice Hall, New Jersey, 1991).

[26] R. Berkovits and S. Feng, *Correlations in coherent multiple scattering*, Physics Reports **238**, 135 (1994).

[27] A. Ioffe and A. Regel, *Non-Crystalline, Amorphous and Liquid Electronic Smiconductors*, Progress in semiconductors **4**, 237 (1960).

[28] A. Genack and J. Drake, *Relationship between Optical Intensity, Fluctuations and Pulse Propagation in Random Media*, Europhysics Letters **11**, 331 (1990).

[29] A. Lysiansky and D. Livdan, *Intensity correlation in wave propagation through random media with internal reflection*, Physics Letters A **170**, 53 (1992).

[30] J. W. Goodman, *Statistical optics* (Wiley, New York, 2000).

[31] *CRC Handbook of Chemistry and Physics, 84th Edition*, edited by D. R. Lide (CRC Press, Boca Raton, 2003).

[32] R. H. Kop, *Time-resolved interferometry on metals and disordered systems* (University of Amsterdam, Amsterdam, 1998).

[33] D. H. Dau, *Diffusion of Light in random media* (University of Amsterdam, Amsterdam, 2000).

[34] J. G. Rivas, labbook and data files (unpublished).

[35] M. van Albada, B. van Tiggelen, A. Lagendijk, and A. Tip, *Speed of Propagation of Classical Waves in Strongly Scattering Media*, Physical Review Letters **66**, 3132 (1991).

[36] H. Schomerus, K. van Bemmel, and C. Beenakker, *Localization-induced coherent backscattering effect in wave dynamics*, Physical Review E **63**, 026605 (2001).

[37] A.Lagendijk, R.Vreeker, and P. de Vries, *Influence of internal reflection on diffusive transport in strongly scattering media*, Physics Letters A **136**, 81 (1989).

[38] J. Zhu, D. Pine, and D. A. Weitz, *Internal reflection of diffusive light in random media*, Physical Review A **44**, 3948 (1991).

[39] E. Akkermans, P. Wolf, and R. Maynard, *Coherent Backscattering of Light in Disordered Media: Analysis of the Peak Line Shape*, Physical Review Letters **56**, 1471 (1986).

Acknowledgments

When I first visited the COPS group, about a year ago, I was completely ignorant of the subject of wave diffusion and the possibilities of time resolved optical measurements. If it were not for the help and great enthusiasm of many people, I would still be.

In particular I would like to thank Willem Vos for his unbridled enthusiasm that persuaded me to join COPS, Ad Lagendijk for many inspiring discussions and for fiercely dissuading me from my initial point of view that diffusion is boring, as well as Boris Bret and Peter Lodahl for their daily supervision and help on both experiment and theory. Furthermore, I thank all members of the COPS group; especially Martijn Wubs for helping me out on theoretical issues, Cock Harteveld for technical support, Raymond Oudeboon for his cheerful presence, Léon Wolderink for always asking me what I was doing, and my roommate Arie Irman.

In the IOMS group I would like to thank René de Ridder and Alfred Driessen for looking at my work from a different point of view and being in my graduation committee.

Finally, I would like to thank Iris for her love, support and patience.

Ivo Vellekoop
Enschede, November 2003